

An implicit boundary finite element method with extension to frictional sliding boundary conditions and elasto-plastic analyses

Kaizhou Lu^{a,b}, William M. Coombs^b, Charles E. Augarde^b, Zhendong Hu^{a,*}

^a*School of Aerospace Engineering and Applied Mechanics, Tongji University, Shanghai, 200092, P.R.C*

^b*Department of Engineering, Durham University, Durham, DH1 3LE, UK*

Abstract

Implicit boundary methods, which enrich the interpolation structure with implicit weight functions, are straightforward methods for the enforcement of Dirichlet boundary conditions. In this article, we follow the implicit boundary method that uses approximate step functions (the step boundary method) developed by Kumar et al. and provide modifications that have several advantages. Roller boundary conditions have wide practical applications in engineering, however, the step boundary method for roller boundary conditions with inclinations has yet to be fully formulated through to the final linear system of equations. Thus we provide a complete derivation that leads to simplified stiffness matrices compared to the original approach, which can be implemented directly in fictitious domain finite element analysis. The approach is then extended, we believe for the first time, to the nonlinear cases of frictional boundary conditions and elasto-plastic material behaviour. The proposed formulation and procedures are validated on a number of example problems that test different aspects of the method.

Keywords: Dirichlet boundary conditions, implicit boundary method, fictitious domain, immersed boundary, frictional boundary, elasto-plasticity

1. Introduction

The discretisation process in the classical finite element analysis requires the mesh to be conforming to the physical domain of interest, which can be tedious, time consuming and computationally expensive, especially when the target domain is irregular in three-dimensions. One of the solutions is to remove the grid, for instance meshless methods [1] which have become well-developed methods that do not require mesh generation. Another alternative that circumvents this non-trivial process is to adopt a non-conforming mesh, first suggested by Peskin [2] in the 1970s who embedded the physical domain in a fixed Cartesian mesh on the background in a fluid-structure interaction problem of heart valves, which became known as the immersed boundary method [3]. The combination of this type of approach with finite element analysis has drawn rapidly growing research interest for the past few years, and has also been referred to as the fictitious domain method [4], the embedded boundary method [5], the cut finite element method [6], the non-conforming mesh method [7], etc. Fictitious domain approaches embed a

*Corresponding author.

Email address: zdhu@tongji.edu.cn (Zhendong Hu)

target physical domain Ω into an extended computational domain Ω_{fict} with a much simpler geometry, such that the problem can be discretised using a structured mesh, for instance, a Cartesian grid. Finite elements near the geometric boundary are cut into two parts as a result of the enlarged domain, while only in the inside part should the quadrature for domain integrals be performed. Hence, schemes for boundary approximation and numerical integration are necessary for these cut elements, for instance, the Finite Cell Method [8] which is a fictitious domain finite element approach equipped with adaptive refinement for integration purposes (and combined with high-order finite elements as well). In [9], techniques for both higher-order boundary representation and numerical integration are developed with the Finite Cell Method.

In finite element analysis with the fictitious domain setting, where the geometric boundary and grid nodes are not guaranteed to coincide, one major difficulty comes from the incorporation of Dirichlet boundary conditions, as the traditional way to impose Dirichlet boundary conditions node-wise is no longer feasible. Although there are approaches, such as the point collocation method that try to enforce boundary conditions in the traditional way, major efforts have been expended on weak imposition methods that incorporate Dirichlet boundary conditions during method formulation. The weak imposition methods of Dirichlet boundary conditions developed so far can be classified in three categories. The first category introduces additional terms to the energy functional and the weak form, and includes the Lagrange multiplier method [10–12], the penalty method [13, 14] and Nitsche’s method [15–17], amongst many descendants of these three well-known methods [18–23]. The Fat Boundary Method [24, 25] fits in the second category, the main idea of which is to split the original problem into sub-problems and solve them iteratively. The approach to be introduced in this article belongs to the third category, known as implicit boundary methods [7], which enrich the interpolation structure with implicit weight functions that incorporate geometric information of the Dirichlet boundary. Detailed reviews of approaches developed to date for the weak imposition of Dirichlet boundary conditions in fictitious domain analysis can be found in [26, 27].

The idea of using implicit boundary functions to satisfy boundary conditions in the finite element method can be traced back to the work of Kantorovich and Krylov [28], which was first referred to as the “implicit boundary method” by Kumar et al. [7]. In this article, we follow the use of this term, and the approach proposed in the same article that uses approximate step functions as implicit boundary functions is referred to as the “step boundary method” [29]. Implicit boundary methods enrich the unknown field interpolation with geometric information such that the unknown field satisfies Dirichlet boundary conditions prior to discretisation, and the normal variational principle for the classical finite element method can be employed without modification. Specifically, the concept is to employ a weighted form for, e.g. the scalar unknown field u in a one-dimensional problem, of the form

$$u = \omega \psi^h \tag{1}$$

where ψ^h is the usual approximation of the unknown field and ω is a \mathcal{C}^1 continuous implicit function (also known as the Dirichlet function) that vanishes on the Dirichlet boundary, and possesses positivity elsewhere in the domain. The early work of Kharrik [30] proved the completeness of the enriched form (1) and Rvachev et al. [31] later developed the R-function method to

1 construct exact implicit functions for general boundary conditions. Shapiro et al. [32] provided
2 theories on automatically constructed, differentiated and integrated R-functions. The weighted
3 extended B-spline (WEB) method, a recent approach of Höllig et al. [33, 34], combined this idea
4 with the B-spline-based finite element method. The multivariate B-splines in the WEB method
5 are defined on a tensor product grid which does not fit the physical domain, and the weighted
6 form is adopted to enrich the B-spline basis functions such that the difficulty of incorporating
7 Dirichlet boundary conditions is overcome. The work of Zhang et al. [35] constructs exact in-
8 homogeneous boundary values using the transfinite interpolation technique, following a similar
9 solution framework.

10 The step boundary method [7], first proposed by Kumar et al. [36], where a particular type
11 of approximate step function serves as the weight function, seems to be inspired by the WEB
12 method. A special scheme for integration is developed because of this step-like weight function,
13 leading to a final solution system that can also be categorised as a distributed penalty method.
14 Since then, the step boundary method has also been extended to combine with B-spline bases
15 [37], and applied to inclusion problems [38], shell-like structures [39], dynamics problems [29] and
16 finite deformation problems in the Material Point Method [40, 41]. The essential concept of the
17 step boundary method is to use the following function, which vanishes on the Dirichlet boundary
18 and rises to unity within a step size ϵ , to weight the regular finite element interpolation:

$$\omega(\phi) = 1 - \max(0, 1 - \phi/\epsilon)^r, \quad (2)$$

19 where $\phi = \text{dist}(\mathbf{x}, \Gamma_D)$ denotes the distance from the boundary. The step size ϵ controls the
20 size of the transition and r controls the smoothness. The function tends to the Heaviside step
21 function in the limit as $\epsilon \rightarrow 0$. This function is also employed in the WEB method [34],
22 although in the step boundary method, ϵ is restricted to be sufficiently small compared to the
23 element feature size, which generates a large gradient normal to the Dirichlet boundary. The
24 displacement inside the area where $\phi \geq \epsilon$ remains unchanged, thereby the weighted Dirichlet
25 functions only affect elements cut by the Dirichlet boundary.

26 Conventional penalty methods are often criticised in terms of the variational inconsistency
27 [17, 42], and approaches like Nitsche's method [15, 17] have been invented to overcome this
28 issue. Due to the penalty-type formulation of the step boundary method, it shares the inconsis-
29 tency of penalty methods, however, the method has several advantages as it provides a physical
30 interpretation for the distributed penalty method, and, incorporates material properties in its
31 formulation. In this article, we provide simplifications to the originally proposed step boundary
32 method along with a complete formulation for roller boundary conditions with arbitrary incli-
33 nation, leading to a system of equations that can be implemented directly, and which is not
34 found in the existing literature. The approach is then extended to frictional sliding boundary
35 conditions and elasto-plastic analyses, both being validated through numerical examples. To
36 the authors' knowledge this is the first time that the step boundary method has been applied
37 to these problems. The layout of the paper is as follows, Section 2 provides an introduction to
38 the implicit boundary finite element discretisation; Section 3 provides detailed derivation of the
39 step boundary method for inclined roller boundary conditions and gives a simplified solution
40 system; some implementation details of the proposed method and the fictitious domain setting

are discussed in Section 4. The extension to include features of frictional sliding and the implementation in elasto-plastic analysis are discussed in Section 5 and Section 6, respectively; a number of numerical examples are presented to validate the proposed approaches in Section 7 and, finally, conclusions are drawn in Section 8.

2. Implicit boundary methods

2.1. Problem statement for linear elasticity

In this article, the formulation is presented based on the fictitious domain finite element method in the two-dimensional case for simplicity, however, the methods are easily extendable to other fictitious domain approaches, and to the three-dimensional case. Linear elasticity is first considered as the model problem with the physical domain $\Omega \in \mathcal{R}^2$, and three boundary conditions are described for the physical domain so that $\partial\Omega = \Gamma_D \cup \Gamma_N \cup \Gamma_T$, as shown in Fig. 1. Ω_{db} in the figure represents elements cut by $\Gamma_D \cup \Gamma_T$, and we further denote that $\Omega_\Gamma = \Omega \cap \Omega_{db}$. Γ_D and Γ_N respectively denote Dirichlet and Neumann boundaries. Γ_T is the roller boundary, where both Dirichlet and Neumann boundary conditions are applied, but in normal and tangential directions respectively. The strong form of the problem is stated as

$$\begin{aligned} -\nabla \cdot \boldsymbol{\sigma} &= \mathbf{b} & \text{in } \Omega, & & \mathbf{u} &= \bar{\mathbf{u}} & \text{on } \Gamma_D, & & \boldsymbol{\sigma} \cdot \mathbf{n} &= \bar{\mathbf{g}} & \text{on } \Gamma_N, \\ \alpha_{1j}^s u_j &= \bar{u}'_1 & \text{on } \Gamma_T & & \text{and} & & \alpha_{2j}^s \sigma_{jk} n_k &= \bar{g}'_2 & \text{on } \Gamma_T, \end{aligned} \quad (3)$$

where \mathbf{u} is the displacement vector, $\boldsymbol{\sigma}$ is the stress tensor, \mathbf{b} is the body force vector, and \mathbf{n} denotes the outward normal unit vector on $\partial\Omega$. $\bar{\mathbf{u}}$ and $\bar{\mathbf{g}}$ are boundary value functions on Γ_D and Γ_N , respectively, \bar{u}'_1 and \bar{g}'_2 are boundary values on Γ_T in respective directions, and $\boldsymbol{\alpha}^s$ is a transformation tensor where $\alpha_{ij}^s = \cos(x'_i, x_j)$ are direction cosines, with dashed quantities being defined in local coordinates with $(\cdot)'_1 := (\cdot)_n$ and $(\cdot)'_2 := (\cdot)_t$. The equations are closed with the compatibility equation $\boldsymbol{\varepsilon} = \frac{1}{2}[\nabla \mathbf{u} + (\nabla \mathbf{u})^T]$ and the constitutive relation $\boldsymbol{\sigma} = \mathbf{E} : \boldsymbol{\varepsilon}$, where \mathbf{E} is the elastic tensor. For conciseness, we still use denotations of Γ_D and Γ_N for integrals on Γ_T which only include quantities defined in normal and tangential directions, respectively.

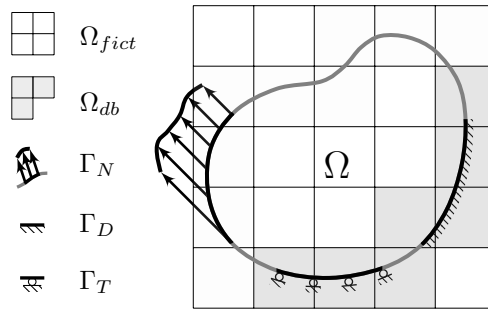


Figure 1: Domain setting of the model problem with boundary conditions.

The solution to Problem (3) is equivalent to the principle of minimum potential energy, that is

$$\Pi(\mathbf{v}) = \int_{\Omega} v_{\varepsilon}(\mathbf{v})d\Omega - \int_{\Omega} \mathbf{v} \cdot \mathbf{b}d\Omega - \int_{\Gamma_N} \mathbf{v} \cdot \bar{\mathbf{g}}d\Gamma \quad \text{and} \quad \mathbf{u} = \arg \min_{\forall v_i \in \mathcal{H}_0^1(\Omega)} \Pi(\mathbf{v}), \quad (4)$$

1 where the strain energy density $v_\varepsilon(\mathbf{v}) = \frac{1}{2}\boldsymbol{\varepsilon}(\mathbf{v}) : \boldsymbol{\sigma}(\mathbf{v})$ in linear elasticity and $\mathcal{H}_0^1(\Omega) = \{v_i \in$
2 $\mathcal{H}^1(\Omega) | \mathbf{v} = \bar{\mathbf{u}} \text{ on } \Gamma_D\}$. The associated weak form statement is: find $u_i \in \mathcal{H}_0^1(\Omega)$ such that

$$3 \int_{\Omega} \boldsymbol{\varepsilon}(\delta \mathbf{u}) : \boldsymbol{\sigma}(\mathbf{u}) d\Omega = \int_{\Omega} \delta \mathbf{u} \cdot \mathbf{b} d\Omega + \int_{\Gamma_N} \delta \mathbf{u} \cdot \bar{\mathbf{g}} d\Gamma, \quad (5)$$

4 where $\delta \mathbf{u}$ denotes the variation of the displacement \mathbf{u} . The preceding principle holds under the
5 assumption that the displacement satisfies Dirichlet conditions in advance, i.e. $v_i \in \mathcal{H}_0^1(\Omega)$,
6 whereas problems arise in the fictitious domain setting in which $v_i \in \mathcal{H}^1(\Omega)$, i.e. there is
7 nowhere to strongly enforce Dirichlet boundary conditions as the discretisation is not aligned
8 with the physical boundary .

9 2.2. Implicit boundary finite element discretisation

10 As introduced above, implicit boundary methods enrich the unknown field approximation
11 using implicit weight functions. It is convenient to formulate the method with matrix notations,
12 whereby the weighted displacement in two-dimensional elasticity is given as

$$13 \mathbf{u} = \mathbf{w} \mathbf{u}_g + \mathbf{u}_a, \quad (6)$$

14 in which the weight matrix $\mathbf{w} = \text{diag}(\omega_x, \omega_y)$, with ω_x or ω_y being either the Dirichlet func-
15 tion ω in (2) if the corresponding direction is fixed (or prescribed) or unity if unconstrained.
16 $\mathbf{u}_g = [u_{x,g}, u_{y,g}]^T$ is the grid unknown and $\mathbf{u}_a = [u_{x,a}, u_{y,a}]^T$ is the function that satisfies the
17 inhomogeneous Dirichlet boundary conditions. The discretisation for the grid unknown is given
18 as $\mathbf{u}_g(\mathbf{x}) = \sum_{j=1}^{n_d} \mathbf{N}_j(\mathbf{x}) \mathbf{u}_{j,g}^e = \mathbf{N}(\mathbf{x}) \mathbf{u}_g^e$, where n_d is the number of element nodes, $\mathbf{N}_j = N_j \mathbf{I}_{2 \times 2}$
19 is the product of the j th shape function and the 2×2 identity matrix, and $\mathbf{u}_{j,g}^e = [u, v]^T$ repre-
20 sents nodal unknowns. The test function $\delta \mathbf{u}_g$ is approximated in the same way, such that the
21 discretisation gives the following expressions of real and virtual displacements

$$22 \mathbf{u} = \mathbf{w} \mathbf{N} \mathbf{u}_g^e + \mathbf{u}_a \quad \text{and} \quad \delta \mathbf{u} = \mathbf{w} \mathbf{N} \delta \mathbf{u}^e. \quad (7)$$

23 Defining a differential operator as

$$24 \mathcal{L} = \begin{bmatrix} \partial/\partial x & 0 \\ 0 & \partial/\partial y \\ \partial/\partial y & \partial/\partial x \end{bmatrix},$$

25 then vectors of real and virtual strains (in Voigt notation) become

$$26 \boldsymbol{\varepsilon}(\mathbf{u}) = [\varepsilon_x, \varepsilon_y, \gamma_{xy}]^T = \mathcal{L}(\mathbf{u}) = \hat{\mathbf{B}} \mathbf{u}_g^e + \mathcal{L}(\mathbf{u}_a) \quad \text{and} \quad \boldsymbol{\varepsilon}(\delta \mathbf{u}) = \mathcal{L}(\delta \mathbf{u}) = \hat{\mathbf{B}} \delta \mathbf{u}_g^e, \quad (8)$$

27 where the strain-displacement matrix $\hat{\mathbf{B}} = \mathcal{L}(\mathbf{w} \mathbf{N})$ contains derivatives of both Dirichlet and
28 shape functions. The Voigt notation vector of the stress becomes

$$29 \boldsymbol{\sigma}(\mathbf{u}) = [\sigma_x, \sigma_y, \tau_{xy}]^T = \mathbf{D} \boldsymbol{\varepsilon}(\mathbf{u}) = \mathbf{D} \hat{\mathbf{B}} \mathbf{u}_g^e + \mathbf{D} \mathcal{L}(\mathbf{u}_a). \quad (9)$$

30 where \mathbf{D} is the elastic matrix. Substituting the strains and the stress into the weak form (5)
31 gives rise to the following system at the element level

$$32 \hat{\mathbf{k}} \mathbf{u}_g^e = \hat{\mathbf{f}} - \mathbf{f}_{ib}, \quad (10)$$

where

$$\hat{\mathbf{k}} = \int_{\Omega^e} \hat{\mathbf{B}}^T \mathbf{D} \hat{\mathbf{B}} d\Omega, \quad \hat{\mathbf{f}} = \int_{\Omega^e} \mathbf{N}^T \mathbf{w} b d\Omega + \int_{\Gamma_N^e} \mathbf{N}^T \mathbf{w} \bar{g} d\Gamma \quad (11)$$

and

$$\mathbf{f}_{ib} = \int_{\Omega^e} \hat{\mathbf{B}}^T \mathbf{D} \mathcal{L}(\mathbf{u}_a) d\Omega, \quad (12)$$

with the superscript $(\cdot)^e$ denoting domains or boundaries within an element. The Dirichlet boundary value term \mathbf{f}_{ib} comes from the product of the virtual strain $\boldsymbol{\varepsilon}(\delta \mathbf{u})$ in (8) and the second term of the stress (9).

Unlike the boundary value function $\bar{\mathbf{u}}$ in the problem statement, \mathbf{u}_a here is defined over the entire physical domain. As what the system of equations (10) solves for is the discretised grid unknown \mathbf{u}_g , the correct displacement \mathbf{u} should be recovered through (6) after solution. Owing to this feature, a smoothly constructed \mathbf{u}_a that satisfies the inhomogeneous Dirichlet boundary conditions leads to a more accurate solution as compared to using a boundary value function approximated on the grid, see e.g. [35]. Implicit boundary methods are straightforward to understand and represent Dirichlet boundary conditions without losing accuracy. However, a smooth weighting function for the whole physical domain is necessary, requiring costly construction techniques for complex geometries, and the weight function gradient needs to be computed where it is non-zero. Moreover, there is no direct way to impose roller boundary conditions in a general implicit boundary method.

The step boundary method, which is the approach we focus on in this article, employs approximate step functions as the implicit weight function, the resulting stiffness matrix is [37]

$$\hat{\mathbf{k}} = \mathbf{k} + \mathbf{k}_2 + \mathbf{k}_2^T + \mathbf{k}_3, \quad (13)$$

where

$$\mathbf{k} = \int_{\Omega^e} \mathcal{L}(\mathbf{N})^T \mathbf{D} \mathcal{L}(\mathbf{N}) d\Omega, \quad (14)$$

$$\mathbf{k}_2 = \int_{\Gamma_D^e} \int_0^\epsilon \text{diag}(\mathbf{w}, \dots, \mathbf{w}) \mathcal{L}(\mathbf{N})^T \mathbf{D} \mathcal{L}(\mathbf{w}) dn \mathbf{N} d\Gamma \quad \text{and} \quad (15)$$

$$\mathbf{k}_3 = \int_{\Gamma_D^e} \mathbf{N}^T \int_0^\epsilon \mathcal{L}(\mathbf{w})^T \mathbf{D} \mathcal{L}(\mathbf{w}) dn \mathbf{N} d\Gamma. \quad (16)$$

It can be seen that $\hat{\mathbf{k}}$ contains a classical finite element stiffness, \mathbf{k} , and additional stiffness matrices \mathbf{k}_2 and \mathbf{k}_3 .

3. Generalised formulation of the step boundary method

3.1. Interpolation structure

Although the idea of extending the method to inclined roller boundary conditions has been introduced in [29], there remains a lack of a complete derivation that can be implemented directly. We provide here a detailed formulation that delivers a solution system that can be easily implemented, along with simplified stiffness matrices.

170 Starting with the local displacement unknown \mathbf{u}' , where the weight matrix is introduced
locally, the enriched field unknown [29] can be expressed as

$$\mathbf{u}' = \mathbf{w}'\mathbf{u}'_g + \mathbf{u}'_a, \quad (17)$$

where $\mathbf{w}' = \text{diag}(\omega_n, \omega_t)$. ω_n or ω_t equals to either the Dirichlet function ω in [2] if the cor-
responding direction is fixed (or prescribed) or unity if unconstrained. Applying coordinate
transformation to [17] between global and local tangential coordinates gives

$$\mathbf{u} = \bar{\mathbf{w}}\mathbf{u}_g + \mathbf{u}_a, \quad (18)$$

175 where $\bar{\mathbf{w}} = \mathbf{T}^T\mathbf{w}'\mathbf{T}$ indicates the modified weight matrix in global coordinates. \mathbf{T} is the matrix
form of the transformation tensor $\boldsymbol{\alpha}^s$ in [3], such that

$$\mathbf{T} = \begin{bmatrix} \cos \theta & \sin \theta \\ -\sin \theta & \cos \theta \end{bmatrix}, \quad (19)$$

where θ is the angle between the outward normal \mathbf{n} and the global x direction. In Eq. [18], the
grid unknown \mathbf{u}_g is first transformed into local coordinates by multiplying \mathbf{T} , weighted by \mathbf{w}'
to separate the contribution of local directions, and transformed back with \mathbf{T}^T .

180 With the same finite element formulation as in the previous section, the only change to the
system of equations [10]-[12] is that $\hat{\mathbf{B}} = \mathcal{L}(\bar{\mathbf{w}}\mathbf{N})$, although calculation of the stiffness matrix
 $\hat{\mathbf{k}}$ and the external force vector $\hat{\mathbf{f}}$ can be further simplified thanks to properties of the step-like
function w , [2].

3.2. Stiffness matrices and the external force

185 After discretisation, the stiffness matrix is integrated within each element. For conciseness,
the $\hat{\mathbf{B}}$ matrix is decomposed at the node level, i.e. $\hat{\mathbf{B}} = [\hat{\mathbf{B}}_1 \hat{\mathbf{B}}_2 \cdots \hat{\mathbf{B}}_{n_d}]$, such that the
decomposed $\hat{\mathbf{B}}_j$ ($j = 1, 2, \dots, n_d$) become

$$\hat{\mathbf{B}}_j = \mathcal{L}(\bar{\mathbf{w}}\mathbf{N}_j) = \underbrace{\mathcal{L}(\mathbf{N}_j)}_{\mathbf{B}_{1j}}\bar{\mathbf{w}} + \underbrace{\mathcal{L}(\bar{\mathbf{w}})}_{\mathbf{B}_{2j}}\mathbf{N}_j, \quad (20)$$

in which \mathbf{B}_{2j} (in two-dimensions) can be expressed as

$$\begin{aligned} \mathbf{B}_{2j} &= \begin{bmatrix} \partial/\partial x & 0 \\ 0 & \partial/\partial y \\ \partial/\partial y & \partial/\partial x \end{bmatrix} \left(\begin{bmatrix} \cos \theta & -\sin \theta \\ \sin \theta & \cos \theta \end{bmatrix} \begin{bmatrix} \omega_n & 0 \\ 0 & \omega_t \end{bmatrix} \begin{bmatrix} \cos \theta & \sin \theta \\ -\sin \theta & \cos \theta \end{bmatrix} \right) \begin{bmatrix} N_j & 0 \\ 0 & N_j \end{bmatrix} \\ &= \begin{bmatrix} \cos \theta & -\sin \theta & 0 & 0 \\ 0 & 0 & \sin \theta & \cos \theta \\ \sin \theta & \cos \theta & \cos \theta & -\sin \theta \end{bmatrix} \begin{bmatrix} \frac{\partial \omega_n}{\partial x} & 0 \\ 0 & \frac{\partial \omega_t}{\partial x} \\ \frac{\partial \omega_n}{\partial y} & 0 \\ 0 & \frac{\partial \omega_t}{\partial y} \end{bmatrix} \begin{bmatrix} \cos \theta & \sin \theta \\ -\sin \theta & \cos \theta \end{bmatrix} \begin{bmatrix} N_j & 0 \\ 0 & N_j \end{bmatrix}. \end{aligned} \quad (21)$$

Taking into account that Dirichlet functions are defined to be constant along the boundary, i.e.,

190 $\partial\omega_n/\partial t = \partial\omega_t/\partial t = 0$, and applying the coordinate transformation, we have

$$\mathbf{B}_{2j} = \underbrace{\begin{bmatrix} \cos\theta & 0 \\ 0 & \sin\theta \\ \sin\theta & \cos\theta \end{bmatrix}}_{\mathbf{n}^T} \begin{bmatrix} \cos\theta & -\sin\theta \\ \sin\theta & \cos\theta \end{bmatrix} \underbrace{\begin{bmatrix} \frac{\partial\omega_n}{\partial n} & 0 \\ 0 & \frac{\partial\omega_t}{\partial n} \end{bmatrix}}_{\mathbf{w}'_{\partial}} \begin{bmatrix} \cos\theta & \sin\theta \\ -\sin\theta & \cos\theta \end{bmatrix} \begin{bmatrix} N_j & 0 \\ 0 & N_j \end{bmatrix}. \quad (22)$$

With the notation $\bar{\mathbf{w}}_{\partial} = \mathbf{n}^T \mathbf{T}^T \mathbf{w}'_{\partial} \mathbf{T}$, $\hat{\mathbf{B}}_j$ becomes

$$\hat{\mathbf{B}}_j = \mathbf{B}_{1j} + \mathbf{B}_{2j} = \mathcal{L}(N_j)\bar{\mathbf{w}} + \bar{\mathbf{w}}_{\partial} N_j. \quad (23)$$

The element stiffness thus can be treated similarly as in the original approach, that is

$$\hat{\mathbf{k}} = \mathbf{k}_1 + \mathbf{k}_2^T + \mathbf{k}_2 + \mathbf{k}_3, \quad (24)$$

where

$$\mathbf{k}_1 = \int_{\Omega^e} \mathbf{B}_1^T \mathbf{D} \mathbf{B}_1 d\Omega, \quad \mathbf{k}_2 = \int_{\Omega^e} \mathbf{B}_1^T \mathbf{D} \mathbf{B}_2 d\Omega \quad \text{and} \quad \mathbf{k}_3 = \int_{\Omega^e} \mathbf{B}_2^T \mathbf{D} \mathbf{B}_2 d\Omega. \quad (25)$$

The Dirichlet function (2) generates the large gradient $\partial\omega/\partial n$ within the narrow banded area near the Dirichlet boundary ($n < \epsilon$) as a result of the small band width, ϵ . It rises to a plateau of unity at the distance ϵ such that $\partial\omega/\partial n = 0$ on the plateau. These properties allow the following simplifications:

- integrals over the problem domain containing $\partial\omega/\partial n$, e.g. \mathbf{k}_2 and \mathbf{k}_3 , can be evaluated in the narrow band in local tangential coordinates;
- the contribution of the Dirichlet function itself within the narrow band is negligible if integrals over the problem domain do not involve $\partial\omega/\partial n$, e.g. \mathbf{k}_1 , $\hat{\mathbf{f}}$; and
- values of shape functions N_j and their derivatives barely vary across the narrow band.

As a result, \mathbf{k}_1 and $\hat{\mathbf{f}}$ become the same as in the classical finite element method, that is

$$\mathbf{k}_1 = \int_{\Omega^e} \mathcal{L}(\mathbf{N})^T \mathbf{D} \mathcal{L}(\mathbf{N}) d\Omega = \mathbf{k} \quad \text{and} \quad \hat{\mathbf{f}} = \int_{\Omega^e} \mathbf{N}^T \mathbf{b} d\Omega + \int_{\Gamma_N^e} \mathbf{N}^T \bar{\mathbf{g}} d\Gamma := \mathbf{f}. \quad (26)$$

\mathbf{k}_2 and \mathbf{k}_3 are matrices containing gradients of the Dirichlet function, which are zero for $n > \epsilon$, so they can be integrated within the narrow band near the Dirichlet boundary in local coordinates.

With the last simplification that N_j barely varies across the band, \mathbf{k}_2 and \mathbf{k}_3 can be integrated in the normal direction and along the boundary separately, and the only two variables to be integrated across the band are $\omega(n)$ and the gradient $\partial\omega(n)/\partial n$. As for \mathbf{k}_2 , we have

$$\begin{aligned} \mathbf{k}_2 &= \int_{\Omega^e} \text{diag}(\underbrace{\bar{\omega}, \dots, \bar{\omega}}_{\text{a total of } n_d}) \mathcal{L}(\mathbf{N})^T \mathbf{D} \bar{\mathbf{w}}_{\partial} \mathbf{N} d\Omega \\ &= \int_{\Omega^e} \frac{\partial\omega}{\partial n} \text{diag}(\bar{\omega}, \dots, \bar{\omega}) \mathcal{L}(\mathbf{N})^T \mathbf{D} \tilde{\mathbf{w}}_{\partial} \mathbf{N} d\Omega, \end{aligned} \quad (27)$$

where we have denoted that $\bar{\mathbf{w}}_\partial = \frac{\partial \omega}{\partial n} \tilde{\mathbf{w}}_\partial$, which means $\tilde{\mathbf{w}}_\partial = \mathbf{n}^T \mathbf{T}^T \text{diag}(\psi'_n, \psi'_t) \mathbf{T}$ with

$$\psi'_i = \begin{cases} 1, & u'_i = \bar{u}'_i, \\ 0, & u'_i \text{ unconstrained,} \end{cases} \quad i = n, t. \quad (28)$$

As components of \mathbf{w}' in (17) equal to either ω or unity, the only combined term that could lead to large values in \mathbf{k}_2 is $\frac{\partial \omega(n)}{\partial n} \omega(n)$, the integration of which over the narrow band width is

$$\int_0^\epsilon \frac{\partial \omega(n)}{\partial n} \omega(n) dn = \frac{1}{2} \omega^2(n) \Big|_0^\epsilon = \frac{1}{2}. \quad (29)$$

As \mathbf{k}_2 really does not contain large penalty values, and taking into account that the banded area of integration is sufficiently narrow, \mathbf{k}_2 becomes negligible compared to \mathbf{k}_3 , which can be derived similarly as

$$\begin{aligned} \mathbf{k}_3 &= \int_{\Omega^e} \mathbf{N}^T \bar{\mathbf{w}}_\partial \mathbf{D} \bar{\mathbf{w}}_\partial \mathbf{N} d\Omega \\ &= \int_{\Omega^e} \mathbf{N}^T \left(\frac{\partial \omega}{\partial n} \right)^2 \tilde{\mathbf{w}}_\partial \mathbf{D} \tilde{\mathbf{w}}_\partial \mathbf{N} d\Omega \\ &= \int_{\Gamma_D^e} \mathbf{N}^T \int_0^\epsilon \left(\frac{\partial \omega}{\partial n} \right)^2 \tilde{\mathbf{w}}_\partial \mathbf{D} \tilde{\mathbf{w}}_\partial dn \mathbf{N} d\Gamma. \end{aligned} \quad (30)$$

In the case of no inclination, where $\theta = 0$, (27) and (30) are equivalent to the original expressions (15) and (16), although \mathbf{k}_2 is neglected in the following.

3.3. Step size and convergence properties

Since the step boundary methods is categorised a penalty-type method, it possesses similar properties, including variational inconsistency, to classical penalty methods, which means the Dirichlet boundary conditions are enforced approximately such that the solution depends directly on the penalty parameter, discussed in detail by Arnold et al. [17]. In other words, the penalty factor β (or ϵ^{-1} in the step boundary method) should be chosen large enough such that the inaccuracy of the imposed boundary condition is negligible compared to the error from finite element discretisation.

Moreover, the acceptable value of β increases with grid refinement in penalty approaches [26]. Babuška [13] proved that the optimal rate of convergence of the order h can be achieved in the energy norm for linear elements when β is taken to be the order of h^{-1} , i.e. $\beta = \eta h^{-1}$, where the constant, η , should be large enough to enforce the required boundary condition and h is the element size, but optimality is lost with such choice of β in the \mathcal{L}^2 norm, or for quadratic elements. For the step boundary method, an empirical choice is to take $\epsilon^{-1} = \eta h^{-2}$ with $\eta = 1 \times 10^3$, i.e. $\epsilon = h^2 \times 10^{-3}$, which is observed to work for both linear and quadratic elements. The convergence properties of the step boundary method are further analysed in more detail in Section 7.1.

3.4. Dirichlet boundary value term

The following locally weighted form for the Dirichlet boundary value \mathbf{u}_a [38] is employed here

$$\mathbf{u}_a' = (\mathbf{I} - \mathbf{w}') \bar{\mathbf{u}}', \quad (31)$$

where $\mathbf{I} = \mathbf{I}_{2 \times 2}$ is the identity matrix, $\bar{\mathbf{u}}$ is the boundary value function in Eq. (3), defined on Γ_D and Γ_T , and $\mathbf{w}' = \mathbf{w}'(n)$ is the same weight matrix as in (17). Applying coordinate transformation to (31) leads to

$$\mathbf{u}_a = \mathbf{T}^T \mathbf{u}_a' = \mathbf{T}^T (\mathbf{I} - \mathbf{w}') \mathbf{T} \bar{\mathbf{u}} = (\mathbf{I} - \bar{\mathbf{w}}) \bar{\mathbf{u}}. \quad (32)$$

The same discretisation as the grid unknown should be used, i.e. $\bar{\mathbf{u}} = \mathbf{N} \bar{\mathbf{u}}^e$, whereby we have

$$\begin{aligned} \mathbf{f}_{ib} &= \int_{\Omega^e} (\mathbf{B}_1 + \mathbf{B}_2)^T \mathbf{D} \mathcal{L}[(\mathbf{I} - \bar{\mathbf{w}}) \mathbf{N}] d\Omega \bar{\mathbf{u}}^e \\ &= \int_{\Omega^e} (\mathbf{B}_1 + \mathbf{B}_2)^T \mathbf{D} (\mathbf{B} - \mathbf{B}_1 - \mathbf{B}_2) d\Omega \bar{\mathbf{u}}^e. \end{aligned} \quad (33)$$

And following similar simplification steps for stiffness matrices in the previous section, \mathbf{B} becomes approximately identical to \mathbf{B}_1 when integrated over the domain and the only term left that is not negligible is

$$\mathbf{f}_{ib} = - \int_{\Omega^e} \mathbf{B}_2^T \mathbf{D} \mathbf{B}_2 d\Omega \bar{\mathbf{u}}^e = -\mathbf{k}_3 \bar{\mathbf{u}}^e. \quad (34)$$

The final finite element system of equations can be written as

$$(\mathbf{k} + \mathbf{k}_3) \mathbf{u}^e = \mathbf{f} + \mathbf{k}_3 \bar{\mathbf{u}}^e, \quad (35)$$

where \mathbf{k} and \mathbf{f} are normal finite element terms in (26) and \mathbf{k}_3 is defined in (30). Of note is that the recovery of displacement is not required after solution, i.e. $\mathbf{u}^e = \mathbf{u}_g^e$, as the small step size of the weight $(1 - \omega)$ makes the weighted boundary value a penalty and no longer influential to nodal unknowns.

4. Numerical implementation

4.1. Integration scheme

Fig. 2 shows a straightforward treatment of the physical boundary $\partial\Omega$, where a piecewise linear approximation $\partial\Omega_h$ is spanned between points where the boundary and the grid intersect. Two and three Gauss points, marked using filled stars, are placed on each segment respectively for bilinear and biquadratic elements. Adaptive refinement or higher order representations of the boundary are available in the literature [9, 43, 44] which improve performance, although this is beyond the scope of this article.

The integration scheme for domain integrals over Ω_{full}^e (elements that lie entirely in the physical domain) remains unchanged. As integrals over elements cut by the boundary should be evaluated within the physical boundary, the physical domain of a cut element, Ω_{cut}^e , is sub-triangulated for integration, while the element itself remains intact. Fig. 2 also displays examples of Gauss points for both bilinear and eight-noded biquadratic elements, where Gauss locations for isoparametric triangular elements are used in each triangular patch, as indicated. Such a strategy for the integration in boundary elements is also found in [19, 45, 46]. A reduced integration scheme (adopted by elasto-plastic analyses in Section 7.5 and 7.6) for quadrilateral element is shown using filled triangles and diamonds for cut and full elements, respectively.

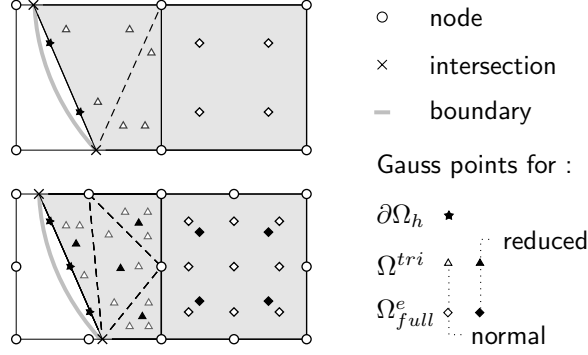


Figure 2: Examples of boundary approximation and integration schemes for linear and eight-noded biquadratic elements.

4.2. Support reactions

Following the quadrature scheme along a Dirichlet boundary segment introduced in Section 4.1, the physical interpretation of \mathbf{k}_3 , (30), can be given by

$$\mathbf{r} = \mathbf{k}_3(\bar{\mathbf{u}}^e - \mathbf{u}^e) = \sum_{m=1}^{n_{gp,e}} \mathbf{N}^T(\boldsymbol{\xi}_m) \mathbf{t}_m^\xi, \quad (36)$$

where \mathbf{r} is the element reaction vector resulting from all boundary segments inside an element, \mathbf{t}_m^ξ is the traction contribution of a Gauss point $\boldsymbol{\xi}_m$ and $n_{gp,e}$ is the number of all boundary Gauss points. The first equality in (36) is concluded from Eq. (35) and the fact that the virtual work of the applied external force and the support reaction should equal the virtual work done by the internal stress, i.e.

$$\mathbf{v}^e \int_{\Omega^e} \mathbf{B}^T \boldsymbol{\sigma}(\mathbf{u}^e) d\Omega = \mathbf{v}^e (\mathbf{f} + \mathbf{r}), \quad (37)$$

which is equivalent to $\mathbf{k}\mathbf{u}^e = \mathbf{f} + \mathbf{r}$.

The computation of the global reaction vector is essential in nonlinear analyses, as support reactions contribute to the algorithmic out-of-balance residual. For convenience, corresponding uppercase letters in the following are used to denote global matrices assembled over all elements, e.g. \mathbf{K}_3 (for the entire system) is assembled from \mathbf{k}_3 (for each element), such that the global reaction vector can be achieved through

$$\mathbf{R} = \mathbf{K}_3(\bar{\mathbf{U}} - \mathbf{U}). \quad (38)$$

Values in the global \mathbf{R} for a single node, e.g. node A in Fig. 3(a), can receive contributions from different boundaries in surrounding elements in a fictitious domain approach. The computation of local support reactions $\mathbf{R}^{(i)}$ on separate boundaries is essential for convergence in analyses with frictional sliding boundaries, as reactions on frictional boundaries should be updated according to the interface constitutive model separately. As a result, the corresponding contribution of a frictional boundary $\mathbf{K}_3^{(i)}$ to the stiffness \mathbf{K}_3 should be formed, e.g. during the quadrature of $\mathbf{K}_3^{(2)}$ in Fig. 3(a), all other Gauss points are excluded except those on the boundary $\langle 2 \rangle$. The product of the stiffness $\mathbf{K}_3^{(i)}$ and the displacement solution gives

$$\mathbf{R}^{(i)} = \mathbf{K}_3^{(i)}(\bar{\mathbf{U}} - \mathbf{U}). \quad (39)$$

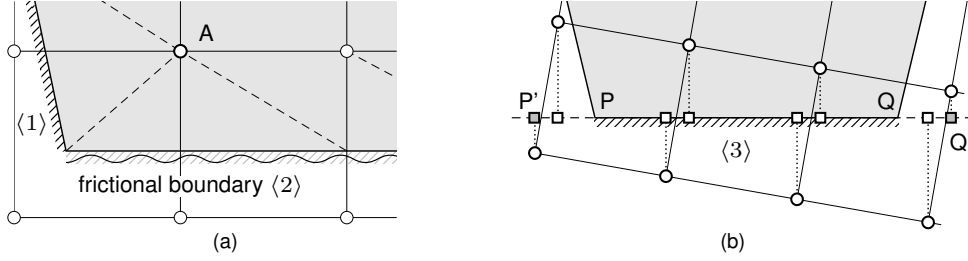


Figure 3: (a) A discretised domain with $\langle 1 \rangle$ full fixation on the left and $\langle 2 \rangle$ the frictional sliding condition at the bottom and (b) projection points (square markers) for reaction forces on a Dirichlet boundary $\langle 3 \rangle$.

The linearisation process in the Newton-Raphson scheme for frictional sliding boundaries requires the evaluation of \mathbf{t}_m^ξ in (36), the traction at boundary Gauss points, such that the tangent stiffness matrix consistent with the reaction update process can be derived. However, for the step boundary method, the recovered \mathbf{t}_m^ξ after solution are often highly oscillatory along a Dirichlet boundary, such that to determine and process frictional sliding status at Gauss points would likely lead to divergence. Such oscillation is also observed in [47] using conventional penalty-type methods. In spite of the unstable tractions, nodal reactions in $\mathbf{R}^{(i)}$ still characterise forces the boundary is subjected to. Nodal reactions can be considered to be forces induced by the constrained boundary at a set of sampling points. Here we have selected the same amount, n_{bn} , of sampling locations ζ_m ($m = 1, 2, \dots, n_{bn}$) as the associated nodes, such that the approximation follows a one-to-one mapping in between, which makes the re-calculation of nodal reaction values convenient after these forces are updated at ζ_m . For instance, sampling locations ζ_m for the boundary $\langle 3 \rangle$ in Fig. 3(b) are defined by the linear mapping from projections of associated nodes on P'Q' (marked by squares) onto PQ. When sampling points from nodes, e.g. nodes R and S, coincide at ξ_m on the boundary, the reactions are combined. In order to retrieve respective nodal reactions again after the force components of \mathbf{r}_m at ξ_m are updated, we split the force by $\mathbf{r}_i = \mathbf{r}_m N_i / (N_R + N_S)$ (i represents R,S), where N_m are shape functions of the two nodes in the element ξ belongs to. The strategy introduced above has been found to be numerically stable for frictional sliding boundary conditions discussed in the following section which needs reaction information for the iterative solver.

One remark is made here regarding the properties of high-order elements, where the equivalent nodal forces associated with a traction are not intuitive in that some of the equivalent nodal forces will act in the opposite direction to the imposed traction, typically the corner nodes for quadratic elements. However, the ratio of normal versus tangential components of nodal reactions, r_n/r_τ , is still reasonably smooth, i.e. the signs of the two components would reverse in conjunction (see, e.g., results in Fig. 19). As the Coulomb law (44) is considered in this article, the friction algorithm is not affected by this non-physical behaviour of high-order elements, as shown in Section 7.3.

5. Frictional sliding boundary conditions

5.1. Linearisation

Considered as an extension to the roller boundary condition, frictional sliding boundary conditions (without an opening mode) limits the shear traction depending on specific friction models and provides more realistic interfaces for problems such as soil-structure interaction in geotechnical engineering. **The proposed approach in this section allows the step boundary formulation to be capable of dealing with roller boundaries with Coulomb friction, and we do not separate the boundary condition and the boundary of the physical domain in the algorithm.** The relevant research topic of frictional sliding on rough rigid interfaces can be deemed as a reduced contact problem, and has been well developed in the traditional finite element framework, see e.g. [48, 49] for details. In the context of fictitious domain approaches, efforts expended to date have mainly followed the pioneering work by Dolbow et al. [50] in the extended finite element method for the modelling of crack growth with frictional contact, e.g. [51, 52]. In [53], a weighted Nitsche’s method is proposed to model frictional sliding on interfaces embedded in background meshes.

For a deformed state with the element displacement vector \mathbf{u}^{e*} and the global \mathbf{U}^* , the discretised weak form to be linearised can be stated as

$$\mathbf{F}^{oob}(\mathbf{U}^*) = \mathbf{F}^{int}(\mathbf{U}^*) - (\mathbf{F}^{ext} + \mathbf{R}(\mathbf{U}^*)) = 0 \quad (40)$$

where \mathbf{F}^{oob} is the global out-of-balance force vector, the global external force $\mathbf{F}^{ext} = \mathbf{F}$ is assembled from (26) and \mathbf{F}^{int} is the global internal force vector assembled from

$$\mathbf{f}^{int} = \int_{\Omega^e} \mathbf{B}^T \boldsymbol{\sigma}(\mathbf{u}^{e*}) d\Omega = \mathbf{k} \mathbf{u}^{e*}. \quad (41)$$

The nonlinearity of frictional boundary conditions comes from the global support reaction \mathbf{R} , (38), assembled from \mathbf{r} , (36). As discussed in Section 4.2, we update reaction forces according to the frictional model at sampling points ζ_m , whereas the stiffness matrix \mathbf{k}_3 is summed up through boundary Gauss points. As the stick-slip status of these sampling points does not represent that of Gauss points, we apply the following algorithmic stiffness matrix once slip is detected that simply releases the boundary tangentially

$$\mathcal{D}\mathbf{r}(\mathbf{u}^{e*}) \cong - \int_{\Gamma_D^e} \mathbf{N}^T \int_0^\epsilon \left(\frac{\partial \omega}{\partial n}\right)^2 \tilde{\mathbf{w}}_\partial^{alg} \mathbf{D} \tilde{\mathbf{w}}_\partial^{alg} dn \mathbf{N} d\Gamma := -\mathbf{k}_3^{alg}, \quad (42)$$

with $\tilde{\mathbf{w}}_\partial^{alg} = \mathbf{n}^T \mathbf{T}^T \text{diag}(1, 0) \mathbf{T}$, which is inconsistent with the reaction update procedure and at the cost of the optimal rate of convergence for the Newton process.

5.2. Coulomb’s friction law

In this article, we adopt the classical Coulomb’s law as the friction model in numerical examples, the flow rule and the yield function of which can be stated in the rate form as

$$\dot{u}_\tau = \dot{\gamma} \frac{t_\tau}{\|t_\tau\|} \quad \text{and} \quad (43)$$

$$\phi_y(t_\tau, t_n) = \|t_\tau\| - \mu t_n, \quad (44)$$

where ϕ_y is the yield function, $\dot{\gamma}$ is the slip rate t_n and t_τ are normal and tangential tractions, respectively, and μ is the coefficient of friction. The Kuhn-Tucker consistency conditions are enforced through

$$\dot{\gamma} \geq 0, \quad \phi_y(t_\tau) \leq 0, \quad \dot{\gamma}\phi_y = 0, \quad (45)$$

which restricts the slip in the yield surface.

As discussed, normal and tangential reaction forces r_n and r_τ at sampling points ζ_m , which are mapped from nodal reactions, are evaluated in replacement of t_n and t_τ in Eqs. (43)-(45). More specifically, we make the assumption that ratio of normal and tangential values r_n/r_τ still describes the physical ratio distribution of tractions along the boundary. On the other hand, nodal reactions (although they might have non-physical signs for high-order elements) are equivalent to the actual distributed tractions along the support, such that when these reactions are scaled in proportion based on the Coulomb law (44) (regardless of their signs, i.e. $r_\tau = \mu r_n$ if violated), we would be able to update the actual amount of nodal reactions which is still equivalent to the distributed tractions the boundary is actually subjected to in each iteration. Thus the implicit return mapping method can be employed in the following procedures, which splits the frictional sliding problem into: (a) an elastic predictor at the trial state, which corresponds Eqs. (46)-(49) in Section 5.3; and (b) a plastic corrector, which gives updated tangential tractions (or forces in our case) on frictional boundaries according to the friction model. A detailed introduction on return mapping algorithm for frictional contact problems can be found in, e.g. [49].

We should point out that the above strategy is a compromised approximation of the traction integration procedure for Eqs. (43)-(45) at Gauss points. This is to circumvent the splitting of each nodal reaction into respective contributions from Gauss points, which very likely leads to divergence [53]. With a relatively fine discretisation, the influence of the approximation in our approach would be insignificant. From our experience, an alternative approach, which employs tractions computed from stresses at Gauss points and integrates the updated tractions into nodal forces, would lead to very slow convergence due to the slight mismatch between the tractions from stresses and the tractions provided by nodal reactions; other strategies of splitting the nodal reactions in different ways are likely to bring about divergence of the iterative algorithm.

5.3. Overall algorithm

The frictional problem is path-dependent, whether to apply the external load in several increments or not depends on specific problems, and using a proportional load curve (\mathbf{F}_j^{ext} for loadstep j) for the external load helps to avoid ambiguity of the real loading process in many cases. Similarly, the prescribed Dirichlet boundary value $\bar{\mathbf{U}}$ is broken into a same number of displacement increments $\Delta_{ls}\bar{\mathbf{U}}_j$. An iterative procedure is developed in each loadstep, where the k th incremental out-of-balance force vector is $\mathbf{F}_{j,(k)}^{oob} = \mathbf{F}_{j,(k)}^{int} - (\mathbf{F}_j^{ext} + \mathbf{R}_{j,(k)})$, and the subscription j is omitted in the following for conciseness. As the boundary value part in the reaction \mathbf{R} is independent of the current deformed state, the entire increment $\Delta_{ls}\bar{\mathbf{U}}$ can be imposed in the first iteration, such that the initial system that solves for $\Delta\mathbf{U}_{(1)}$ becomes

$$(\mathbf{K} + \mathbf{K}_{3,(0)})\Delta\mathbf{U}_{(1)} = \mathbf{F}_{(0)}^{oob} + \mathbf{K}_{3,(0)}\Delta_{ls}\bar{\mathbf{U}}, \quad (46)$$

where $\mathbf{K}_{3,(0)}$ is the stiffness with full prescription on frictional boundaries and $\mathbf{F}_{(0)}^{int}$ and $\mathbf{R}_{(0)}$ inherit the values from the last loadstep. The solution gives global and local trial reactions $\mathbf{R}_{(1)}^{trial}$ and $\mathbf{R}_{(1)}^{trial,(i)}$ as

$$\mathbf{R}_{(1)}^{(\cdot),trial} = \mathbf{R}_{(0)}^{(\cdot)} + \mathbf{K}_{3,(0)}^{(\cdot)} (\Delta l_s \bar{\mathbf{U}} - \Delta \mathbf{U}_{(1)}). \quad (47)$$

$\mathbf{R}_{(1)}^{(i),trial}$ is then transformed to the sampling points, inserted into the return mapping algorithm such that the updated $\mathbf{R}_{(1)}^{(i)}$ can be obtained, and $\mathbf{R}_{(1)}$ is updated accordingly and integrated into $\mathbf{F}_{(1)}^{oob}$. The initially prescribed segment is set to be released tangentially if the criteria in (45) for the yield function (44) at any associated sampling point is violated, that is, $\mathbf{k}_3 = \mathbf{k}_3^{alg}$ in (42), such that the global $\mathbf{K}_{3,(k)}^{alg}$ keeps being updated after the first iteration, and the system of equations becomes

$$(\mathbf{K} + \mathbf{K}_{3,(k-1)}^{alg}) \Delta \mathbf{U}_{(k)} = \mathbf{F}_{(k-1)}^{oob}, \quad k > 1. \quad (48)$$

Due to that \mathbf{K}_3^{alg} changes during the iteration procedure, subsequent trial reactions are calculated in an additive way as

$$\mathbf{R}_{(k)}^{(\cdot),trial} = \mathbf{R}_{(k-1)}^{(\cdot)} - \mathbf{K}_{3,(k)}^{alg,(\cdot)} \Delta \mathbf{U}_{(k)}, \quad k > 1. \quad (49)$$

The current displacement is calculated through the summation of incremental solutions, i.e. $\mathbf{U}_{j,(k)} = \mathbf{U}_{j,(0)} + \sum \Delta \mathbf{U}_{j,(k)}$. The overall pseudo-code of the step boundary algorithm for frictional sliding boundary conditions is included in the Newton-Raphson framework together with elasto-plastic analysis in Section 6 (see Algorithm 1).

6. Elasto-plasticity

6.1. Linearisation

In elasto-plastic analysis, \mathbf{F}^{ext} in the discretised weak form (40), which contains the body force and the traction on the Neumann boundary, is not dependent on the current deformed state, such that it remains constant throughout a certain load increment, whereas both \mathbf{F}^{int} and \mathbf{R} in Eq. (40) are to be linearised, that is

$$\mathcal{D} \mathbf{f}^{int}(\mathbf{u}^{e*}) = \int_{\Omega^e} \mathbf{B}^T \mathbf{D}^{alg} \mathbf{B} d\Omega := \mathbf{k}^{alg} \quad \text{and} \quad (50)$$

$$\mathcal{D} \mathbf{r}(\mathbf{u}^{e*}) = - \int_{\Gamma_D} \mathbf{N}^T \int_0^\epsilon \left(\frac{\partial \omega}{\partial n} \right)^2 \tilde{\mathbf{w}}_{\partial} \mathbf{D}^{alg} \tilde{\mathbf{w}}_{\partial} dn \mathbf{N} d\Gamma := -\mathbf{k}_3^{alg}, \quad (51)$$

with \mathbf{D}^{alg} being the algorithmic tangent [54] of the linearised constitutive model. Hence, the linearisation of the out-of-balance force (40) with respect to the incremental global displacement $\Delta \mathbf{U}$ can be written as

$$\begin{aligned} \mathcal{L}_u(\mathbf{U}^*, \Delta \mathbf{U}) &= \mathbf{F}^{oob}(\mathbf{U}^*) + \mathcal{D}[\mathbf{F}^{int}(\mathbf{U}^*) - \mathbf{R}(\mathbf{U}^*)][\Delta \mathbf{U}] \\ &= \mathbf{F}^{oob}(\mathbf{U}^*) + (\mathbf{K}^{alg} + \mathbf{K}_3^{alg}) \Delta \mathbf{U}^e, \end{aligned} \quad (52)$$

where \mathbf{K}^{alg} and \mathbf{K}_3^{alg} are respectively assembled from \mathbf{k}^{alg} and \mathbf{k}_3^{alg} , and the achieved stiffness matrices are consistent with the stress integration procedure. This linearised elasto-plasticity problem can then be solved using the classical Newton-Raphson scheme, details of which can be found in, e.g. [55].

6.2. Implicit stress integration

For the classical rate formulation of elasto-plasticity, governing equations are integrated subjected to the Kuhn-Tucker condition (see, e.g. [56] for details). As a result, starting from an initial state in the finite element framework with a known elastic strain $\boldsymbol{\varepsilon}_{(k-1)}^E$, which is subjected to a strain increment $\Delta\boldsymbol{\varepsilon}_{(k)}$, we need the update of the elastic strain $\boldsymbol{\varepsilon}_{(k)}^E$ or equivalently the stress $\boldsymbol{\sigma}_{(k)}$. A detailed review of stress integration schemes is provided in [57], amongst others. The implicit return mapping method, which is employed here, has relatively high accuracy for a given numerical effort, particularly when large strain increments are applied. It splits the stress integration problem into two parts:

(a) an elastic predictor at the trial state

$$\boldsymbol{\sigma}^{trial} = \mathbf{D}\boldsymbol{\varepsilon}^{trial,E} = \mathbf{D}(\boldsymbol{\varepsilon}_{(k-1)}^E + \Delta\boldsymbol{\varepsilon}_{(k)}); \quad \text{and} \quad (53)$$

(b) a plastic corrector

$$\boldsymbol{\sigma}_{(k-1)} = \mathbf{D}\boldsymbol{\varepsilon}_{(k)}^E = \mathbf{D}(\boldsymbol{\varepsilon}^{trial,E} - \Delta\boldsymbol{\varepsilon}^P), \quad (54)$$

where $\Delta\boldsymbol{\varepsilon}^P$ is the incremental plastic strains over the return path, and $(\cdot)^E$ and $(\cdot)^P$ denote elastic and plastic parts of the quantity respectively. Throughout the article, the implicit backward Euler stress integration scheme is used, see, e.g. [57] for details.

6.3. Overall algorithm

The Quasi-Newton scheme for frictional boundary conditions using the step boundary method is compatible with elasto-plastic analysis, where Eqs. (46)-(49) still apply, but \mathbf{K} should be replaced by the incremental $\mathbf{K}_{(k)}^{alg}$, assembled from \mathbf{k}^{alg} in (50), and $\mathbf{K}_{3,(k)}$, assembled from \mathbf{k}_3^{alg} in (51). Moreover, when combined features of both frictional boundary conditions and elasto-plasticity are considered, \mathbf{k}_3^{alg} can be given as

$$\mathbf{k}_3^{alg} = \int_{\Gamma_D^e} \mathbf{N}^T \int_0^\epsilon \left(\frac{\partial\omega}{\partial n}\right)^2 \tilde{\mathbf{w}}_\partial^{alg} \mathbf{D}^{alg} \tilde{\mathbf{w}}_\partial^{alg} dn \mathbf{N} d\Gamma, \quad (55)$$

which is a straightforward combination of Eqs. (42) and (51).

The following normalised out-of-balance force residual is used to determine convergence after the k -th iteration

$$e_{j,(k)}^{oob} = \frac{\|\mathbf{F}_{j,(k)}^{oob}\|_{\mathcal{L}^2}}{\|\mathbf{F}_j^{ext} + \mathbf{R}_{j,(k)}\|_{\mathcal{L}^2}}, \quad (56)$$

typically set to 1×10^{-8} in this article. The pseudo-code of the Newton-Raphson scheme in loadstep j is shown in Algorithm 1.

Algorithm 1 Pseudo-code for the loadstep j of the Newton process

```

1: set  $k = 0$ ; initialise variables  $[\cdot]_{(0)}$ ; set  $\mathbf{F}^{ext}$  and  $\Delta_{ls}\bar{\mathbf{U}}$  of the current loadstep;
2: initialise  $\mathbf{F}_{(0)}^{oob} = \mathbf{F}^{ext} + \mathbf{R}_{(0)} + \mathbf{K}_{3,(0)}^{alg}\Delta\bar{\mathbf{U}}^{ls}$ ;  $tol = 1 \times 10^{-8}$ ;  $e_{(0)}^{oob} = 1.0$ ;
3: while ( $e_{(k)}^{oob} > tol$ ) do
4:    $k = k + 1$ ;
5:   solve for  $\Delta\mathbf{U}_{(k)} = (\mathbf{K}_{(k-1)}^{alg} + \mathbf{K}_{3,(k-1)}^{alg}) \setminus \mathbf{F}_{(k-1)}^{oob}$ ;
6:   update displacements  $\mathbf{U}_{(k)} = \mathbf{U}_{(k-1)} + \Delta\mathbf{U}_{(k)}$  and  $\Delta_{ls}\mathbf{U}_{(k)} = \mathbf{U}_{(k)} - \mathbf{U}_{(0)}$ ;
7:   compute trial reactions  $\mathbf{R}_{(k)}^{trial}$  and  $\mathbf{R}_{(k)}^{trial,(i)}$ ;
8:   for (sampling points  $\zeta_m$ ) do
9:     compute: reaction forces  $r_{n,(k)}$  and  $r_{\tau,(k)}^{trial}$  mapped from  $\mathbf{R}_{(k)}^{trial,(i)}$ ;
10:    initialise an indicator  $\Psi_m = 0$ ;
11:    if ( $\phi_y(r_\tau, r_n) > 0$ ) then
12:      map return  $r_{\tau,(k)}$ ; set  $\Psi_m = 1$  to form  $\mathbf{k}_{3,(k)}^{alg}$  later;
13:    end if
14:  end for
15:  update reactions  $\mathbf{R}_{(k)}^{(i)}$  and  $\mathbf{R}_{(k)}$  accordingly;
16:  for (full elements or triangular patches) do
17:    for (Gauss points) do
18:      compute  $\Delta_{ls}\boldsymbol{\varepsilon}_{(k)}$  from  $\Delta_{ls}\mathbf{U}_{(k)}$ ;
19:      backward Euler stress integration:
20:      - inputs:  $\boldsymbol{\varepsilon}_{(0)}^E$  and  $\boldsymbol{\varepsilon}_{(k)}^{trial,E} = \boldsymbol{\varepsilon}_{(0)}^E + \Delta_{ls}\boldsymbol{\varepsilon}_{(k)}$ ;
21:      - outputs:  $\mathbf{D}_{(k)}^{alg}$ ,  $\boldsymbol{\sigma}_{(k)}$  and  $\boldsymbol{\varepsilon}_{(k)}^E$ ;
22:      form and assemble  $\mathbf{f}_{(k)}^{int}$ ,  $\mathbf{k}_{(k)}^{alg}$ ;
23:    end for
24:    form and assemble  $\mathbf{k}_{3,(k)}^{alg}$  on boundary segments;
25:  end for
26:  update  $\mathbf{F}_{(k)}^{oob} = \mathbf{F}_{(k)}^{int} - (\mathbf{F}^{ext} + \mathbf{R}_{(k)})$  and  $e_{(k)}^{oob} = \|\mathbf{F}_{(k)}^{oob}\|_{\mathcal{L}^2} / \|\mathbf{F}^{ext} + \mathbf{R}_{(k)}\|_{\mathcal{L}^2}$ ;
27: end while

```

7. Numerical examples

This section provides numerical validations for the proposed method. The performance of linear-elastic benchmarks in this section is assessed using error measures based on analytical solutions, where relative errors in \mathcal{L}^2 and energy norms for displacement and stress results are respectively defined as

$$e_u = \frac{\|\mathbf{u}^h - \mathbf{u}^a\|_{\mathcal{L}^2(\Omega)}}{\|\mathbf{u}^a\|_{\mathcal{L}^2(\Omega)}} = \sqrt{\frac{\int_{\Omega} \|\mathbf{u}^h - \mathbf{u}^a\|^2 d\Omega}{\int_{\Omega} \|\mathbf{u}^a\|^2 d\Omega}} \quad \text{and} \quad (57)$$

$$e_\sigma = \frac{\|\boldsymbol{\sigma}^h - \boldsymbol{\sigma}^a\|_{\mathcal{E}(\Omega)}}{\|\boldsymbol{\sigma}^a\|_{\mathcal{E}(\Omega)}} = \sqrt{\frac{\int_{\Omega} (\boldsymbol{\varepsilon}^h - \boldsymbol{\varepsilon}^a) : (\boldsymbol{\sigma}^h - \boldsymbol{\sigma}^a) d\Omega}{\int_{\Omega} \boldsymbol{\varepsilon}^a : \boldsymbol{\sigma}^a d\Omega}}, \quad (58)$$

where superscripts $(\cdot)^h$ and $(\cdot)^a$ denote the finite element and analytical solutions, respectively.

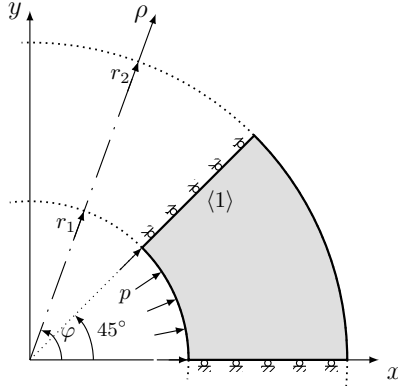


Figure 4: Circular annulus expansion problem with boundary conditions.

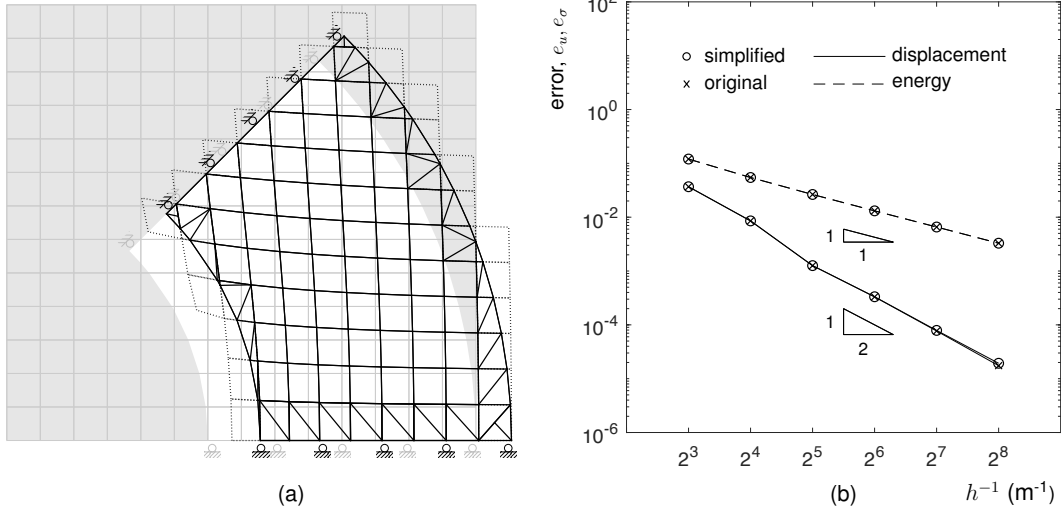


Figure 5: Circular annulus expansion: (a) deformation computed with $\epsilon = 1 \times 10^{-6}$ m and $h = 0.0625$ m and (b) logarithmic errors versus grid refinement obtained with (original) and without (simplified) k_2 .

7.1. Circular annulus expansion

The first example analyses the plane stress expansion of a circular annulus with internal and external radii $r_1 = 0.5$ m and $r_2 = 1$ m, respectively, subjected to internal pressure $p = 0.1$ kPa. The material is assumed to be linear isotropic elastic, with a Young's modulus of $E = 1$ kPa and a Poisson's ratio of $\nu = 0.3$. Due to symmetry, an eighth of the annulus is modelled so as to create an immersed edge with the inclined roller boundary condition, as shown in Fig. 4. The problem is discretised in the fictitious background domain using bilinear square elements. The deformation of the internally pressured annulus is shown in Fig. 5(a), obtained using elements with $h = 0.0625$ m, with the grid feature size h being the side length of these square elements. Each deformed cut element is displayed in two parts, one of which inside the domain is shown with the triangulation by solid black lines, and the outside part is shown by dotted lines.

For empirical choices with bilinear elements, ϵ should decrease in proportion to h to ensure optimal convergence in the energy norm error e_σ with grid refinement, and in proportion to h^2 for the \mathcal{L}^2 error e_u ; here, we have used a fixed $\epsilon = 1 \times 10^{-6}$ m which is small enough for all refined

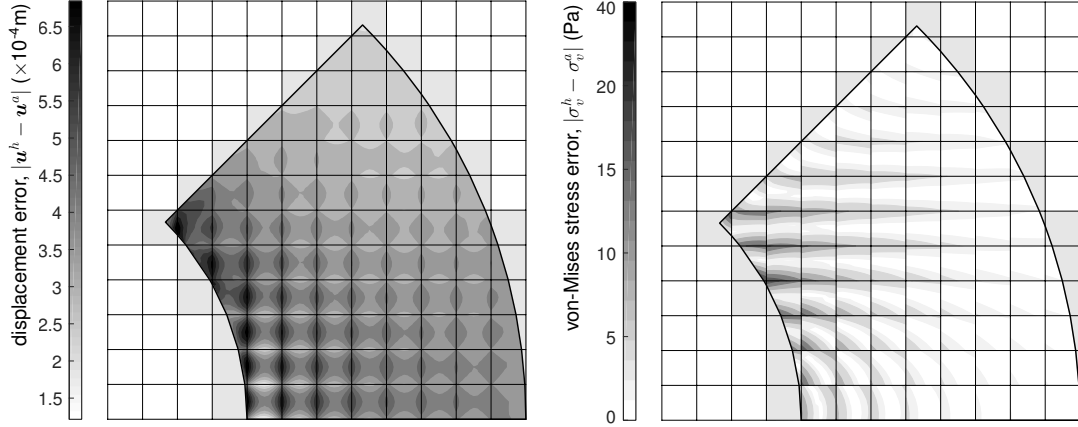


Figure 6: Error contours of the step boundary method implementation ($\epsilon = 1 \times 10^{-6}$ m, $h = 0.0625$ m) for the circular annulus expansion problem.

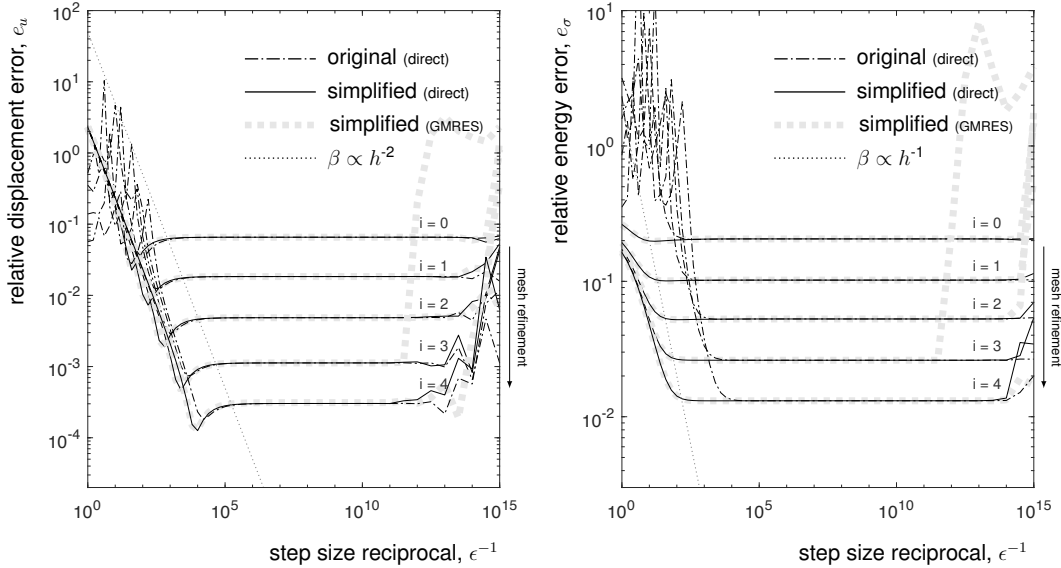


Figure 7: Error plots against the reciprocal of the step size and with uniform grid refinement for the circular annulus expansion problem, where i is the refinement coefficient such that $h = 2^{-(i+3)}$ m, and, obtained using the original formulation (direct solver only) and the simplified formulation (direct and iterative GMRES solvers).

grids employed in this example. The error plots in Fig. 5(b) show optimal rates of convergence in both \mathcal{L}^2 and energy norms, where the results obtained from original (including k_2) and simplified formulations are nearly identical. Fig. 6 shows absolute errors of both displacement and von-Mises stress in contour plots, with $h = 0.0625$ m. Errors are generally larger at the internal Neumann boundary than at the outer edge, and relatively large errors are measured especially where only a small fraction of an element is integrated.

We now carry out a parametric analysis that tests errors with respect to the reciprocal of the parameter ϵ , varying from 0.1 to 10^{15} . The left and right of Fig. 7 illustrate error plots in \mathcal{L}^2 displacement and energy norms, respectively. Each curve in the figure, labelled with the refinement factor i ($i = 0, 1, \dots$), shows the parametric behaviour of the methods (the original formulation and the proposed simplification) obtained using a fixed discretisation which

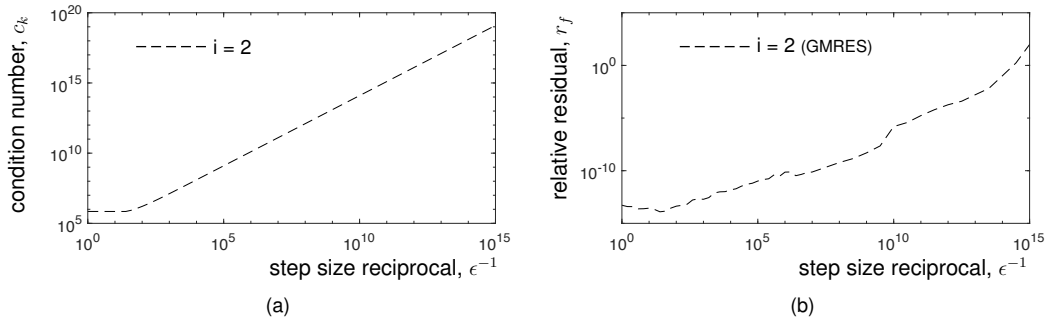


Figure 8: Circular annulus expansion: illustrations of (a) the condition number of the global stiffness matrix against the reciprocal of the step size, and, (b) the relative residual, $r_f = \|\mathbf{F} - (\mathbf{K} + \mathbf{K}_3)\mathbf{U}\|/\|\mathbf{F}\|$, of the GMRES solution against the reciprocal of the step size, with the refinement coefficient $i = 2$.

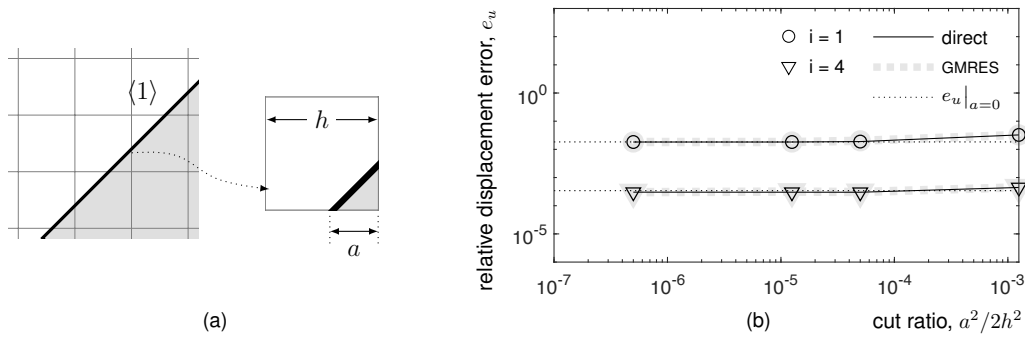


Figure 9: (a) Enlarged boundary $\langle 1 \rangle$ labelled in Fig. 5 and the illustration of a cut element with a small cut ratio; (b) displacement error plot for a selection of discretisation designed to contain pathologic cut elements. The figure shows results obtained using direct and GMRES solvers, with a fixed step size of $\epsilon = 1 \times 10^{-10}$ m.

$h = 2^{-(i+3)}$, solved using both direct and iterative GMRES [58] methods. The errors on the left hand end of the curves of the simplified formulation reduce with respect to decrease of the step size, which follows the typical behaviour of penalty-type approaches, i.e. the boundary conditions are imposed approximately such that the solution is improved with an increased penalty value, as discussed above in Section 3.3. In the original approach, fluctuations in error plots are observed where ϵ^{-1} are small, because the magnitude of ϵ^{-1} becomes similar to the components of k_2 . With a further decrease of ϵ , the behaviours of the original and simplified methods become nearly identical, where errors of both approaches converge to a stage where the finite element discretisation becomes the predominant factor that decides the overall accuracy. The divergence at the right hand ends of the error curves results from ill-conditioning of the global stiffness matrix.

Fig. 7 also displays nearly identical behaviours between direct and GMRES solutions, including the critical step size ϵ_{ic} at which errors start to diverge on the right. In Fig. 8, we illustrate the parametric results of the condition number r_k and the residual $\|\mathbf{F} - (\mathbf{K} + \mathbf{K}_3)\mathbf{U}\|/\|\mathbf{F}\|$ of the GMRES solution (obtained with the grid of $i = 2$), both increasing with respect to the growth in ϵ^{-1} . However, the increasing condition number does not influence the solution until a critical stage, where the error induced by the ill-conditioning becomes no longer negligible compared to that of the finite element method, corresponding to ϵ_{ic} described above for Fig. 7. One remark

is that the GMRES results of $i = 3$ in Fig. 7 diverge more drastically than those of the direct solver, which implies that there exist other factors influencing the errors in this case, but the critical ϵ_{ic} still matches where the solid curve of the displacement error starts to diverge.

As long as the parameter is chosen from the plateau, the same rate of convergence as the classical finite element method can be assured, but the plateau moves rightwards in a certain rate with respect to mesh refinement, as shown in Fig. 7. To show this moving rate with h-refinement, an initial coarse grid with $h_0 = 0.25$ is uniformly refined, with the element size h being halved each time, such that $h = h_0 \times 2^{-i}$ after the i th refinement. Reference lines of $\beta \propto h^{-2}$ and $\beta \propto h^{-1}$ are plotted, respectively, for displacement and energy errors. The reference line matches the moving trend of where the plateau of the energy error starts, which justifies the prediction of Babuška discussed in Section 3.3, while the starting point of the plateau of the displacement error is observed to move in a rate slightly slower than $\beta \propto h^{-2}$.

The boundary $\langle 1 \rangle$ in this model with the inclination of 45° allows the construction of a discretisation with a selection of cut elements that contain small portions of the physical domain, as illustrated in Fig. 9(a). Previously discussed results are obtained by setting $a = 0$, and here we control the cut ratio so as to study the influence of pathologic cuts to our calculations. Fig. 9(b) shows errors for two meshes, $i = 1, 4$, plotted against the cut ratio $a^2/2h^2$. The results are computed using direct (solid lines) and GMRES (dotted grey lines) solvers, and, the black dotted lines represent the errors obtained with $a = 0$. It demonstrates that when the cut ratio approaches as small as 4×10^{-7} , the presented results are still not affected in this case, in other words, the condition of the stiffness matrices is acceptable. For more discussion on this topic, readers are referred to the existing literature, e.g. [7] removes elements with a cut ratio less than 5% to ensure stability; researches that offer stabilisation strategies for spline based methods are found in [33, 45, 59].

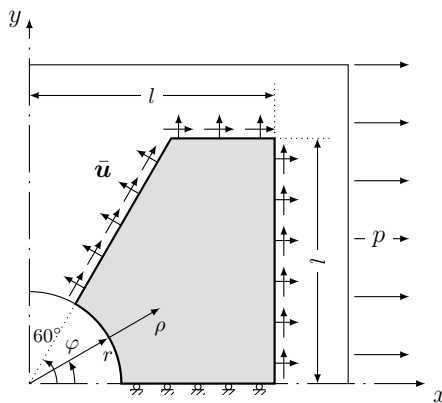


Figure 10: A quadrant of the infinite tensile plate and the 60° computational model (grey area) with boundary conditions.

7.2. Tension in a perforated infinite plate

This example analyses the plane stress tension in an infinite plate with a circular hole of radius $r = 0.5\text{m}$ in the centre, subjected to uni-directional in-plane far-field tension of $p = 0.1\text{kPa}$. The material is assumed to be linear isotropic elastic, with a Young's modulus of

1
2
3
4
5
6
7
8
9
10
11
12
13
14
15
16
17
18
19
20
21
22
23
24
25
26
27
28
29
30
31
32
33
34
35
36
37
38
39
40
41
42
43
44
45
46
47
48
49
50
51
52
53
54
55
56
57
58
59
60
61
62
63
64
65

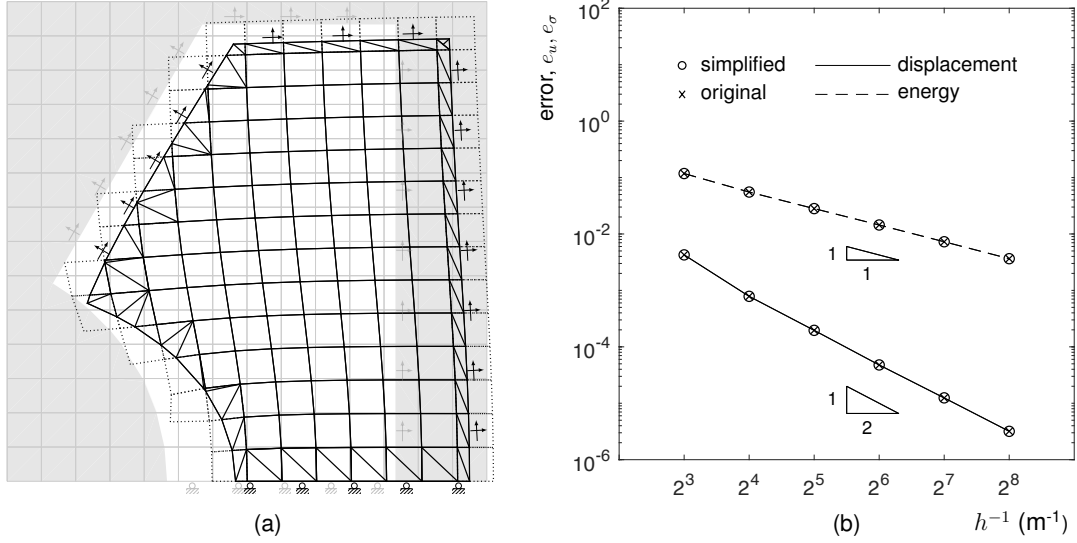


Figure 11: Tension in the perforated plate: (a) deformation computed with $\epsilon = 1 \times 10^{-6}$ m and $h = 0.075$ m and (b) logarithmic errors versus grid refinement obtained with (original) and without (simplified) k_2 .

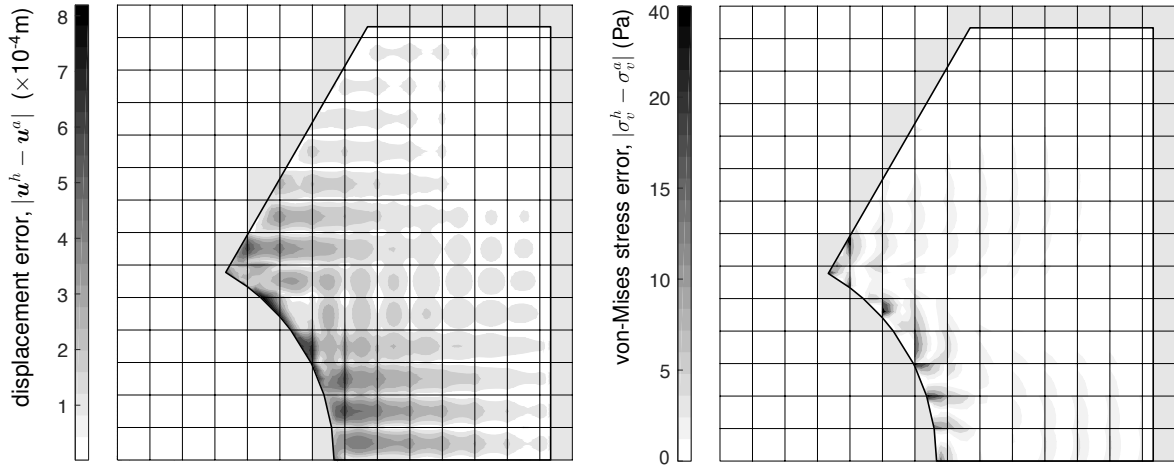


Figure 12: Error contours of the step boundary method implementation ($\epsilon = 1 \times 10^{-6}$ m, $h = 0.075$ m) for the infinite tensile plate problem.

$E = 1$ kPa and a Poisson's ratio of $\nu = 0.3$. The analytical displacement field of the problem is given as [60]

$$\begin{aligned}
 u_x(\rho, \varphi) &= \frac{1 + \nu}{E} p \left(\frac{\rho}{1 + \nu} \cos \varphi + \frac{2r^2}{(1 + \nu)\rho} \cos \varphi + \frac{r^2}{2\rho} \cos 3\varphi - \frac{r^4}{2\rho^3} \cos 3\varphi \right) \quad \text{and} \\
 u_y(\rho, \varphi) &= \frac{1 + \nu}{E} p \left(\frac{-\nu\rho}{1 + \nu} \sin \varphi - \frac{(1 - \nu)r^2}{(1 + \nu)\rho} \sin \varphi + \frac{r^2}{2\rho} \sin 3\varphi - \frac{r^4}{2\rho^3} \sin 3\varphi \right),
 \end{aligned}
 \tag{59}$$

which allows the computation of a 60° portion (with $l = 1$ m), shown in Fig. (10): apart from the homogeneous Neumann boundary at $\rho = r$, displacement is prescribed on the rest of the boundaries (including a roller boundary condition at the bottom) to investigate the performance of the proposed method on non-uniform inhomogeneous Dirichlet boundaries. Bilinear square elements are used to discretise the fictitious domain, and the deformation after solution is shown in Fig. 11(a), obtained using elements with $h = 0.075$ m.

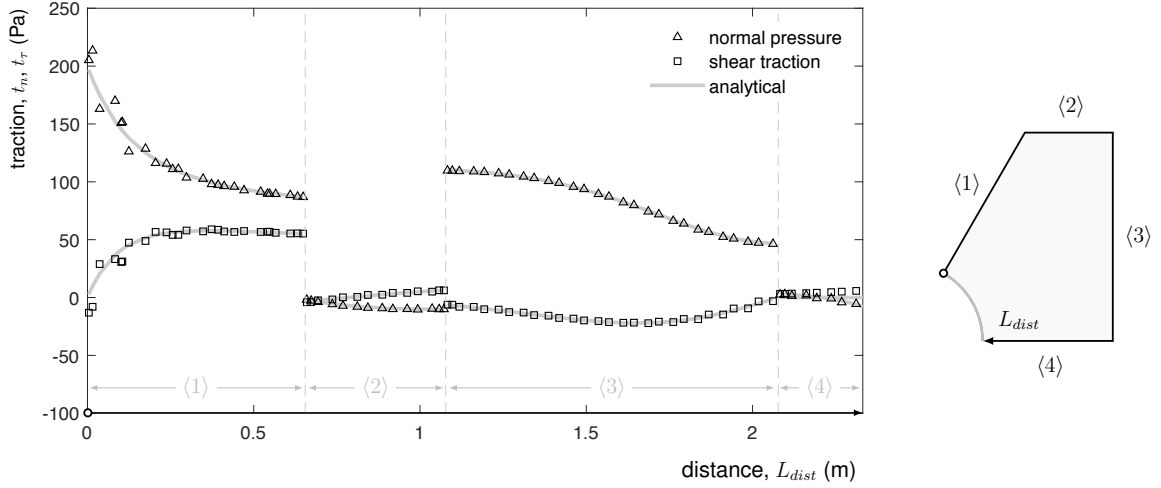


Figure 13: Tension in the perforated plate ($\epsilon = 1 \times 10^{-6}$ m, $h = 0.075$ m): normal pressure and shear traction results along Dirichlet and roller boundaries.

Fig. 11(b) demonstrates again that the simplified formulation gives identical results to the original approach when the step size is small enough to neglect the effect of k_2 , where optimal rates of convergence in both \mathcal{L}^2 and energy norms are observed with uniform refinement, obtained again with a fixed $\epsilon = 1 \times 10^{-6}$ m. Fig. 12 shows absolute error contours obtained with $h = 0.075$ m. Large values of both displacement and stress errors are measured near the free boundary, which is due to the integration scheme and the piecewise linear boundary representation. Fig. 13 shows normal and shear tractions along Dirichlet and roller boundaries and calculated from stress data, which demonstrates good agreement with the analytical solution. The continuity of stresses is one order less than the \mathcal{C}^0 continuous displacement, such that discontinuities occur across element boundaries, such that slight oscillations, relatively more evident on the inclined boundary $\langle 1 \rangle$, are observed in this traction result.

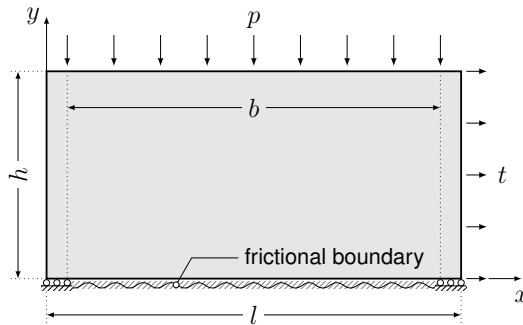


Figure 14: Problem setting of the elastic block sliding on a frictional boundary.

7.3. Block sliding on a frictional boundary

For frictional boundary conditions, we first analyse the problem of a plane strain block sliding on a rigid rough surface. First analysed by Oden et al. [61], this problem was subsequently

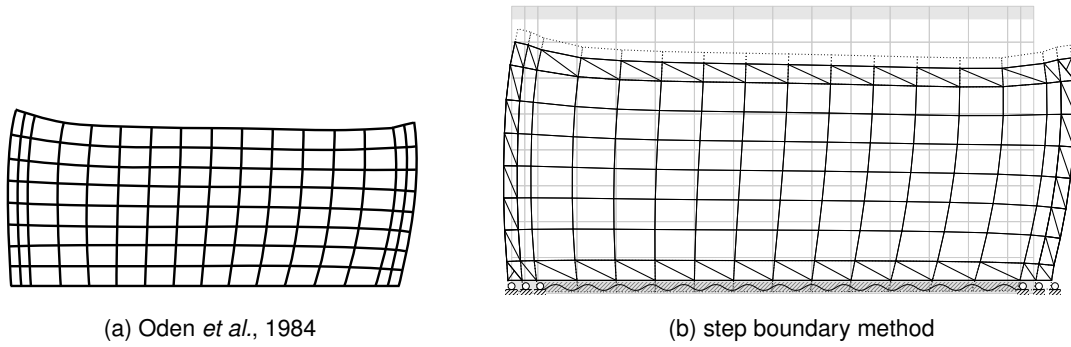


Figure 15: Final deformations of the sliding block problem: (a) reproduced result of Oden et al. [61] and (b) the presenting step boundary method, mesh I.

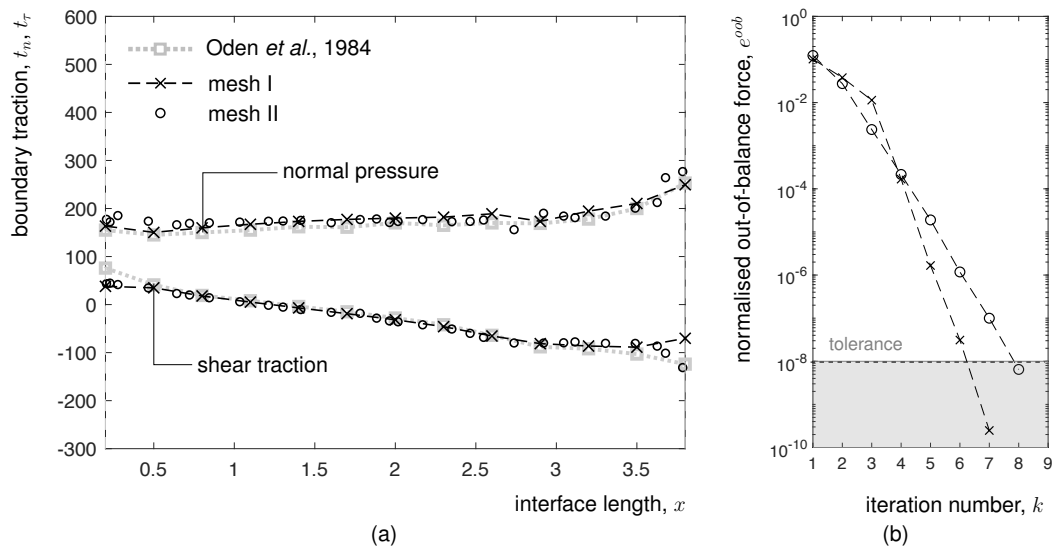


Figure 16: Sliding block problem: (a) normal pressure and shear stress along the frictional boundary and the comparison with existing results and (b) normalised out-of-balance force residual versus iteration number.

analysed in a number of works [53, 62, 63] and serves as a benchmark for frictional interface problems. The block has a length of $l = 4$ units and a height of $h = 2$ units, and is placed on a rough surface with the Coulomb friction coefficient $\mu = 0.5$, subjected to distributed pressures comprising a compression of $p = 200$ units on the top and a traction of $t = 60$ units which pulls the block on its very right side. The compressive load on the top is uniformly distributed over the length of $b = 3.6$ units in the middle, which leaves two corners free from vertical loads, and two homologous sections at the bottom are set up as frictionless rollers, as shown in Fig. [14]. The material is assumed to be linear isotropic elastic, with a Young's modulus of $E = 1000$ units and a Poisson's ratio of $\nu = 0.3$. In accordance with [62], the solution to this problem can be obtained with a single load increment.

Here bilinear elements are first adopted to discretise the problem domain, with both bottom and top physical boundaries being immersed, as shown in Fig. [15](b), where grey shaded regions indicate the void part of elements cut by the boundary. The discretisation is plotted together with the final deformation, and along with Fig. [15](a), the reproduced result of Oden et al. [61].

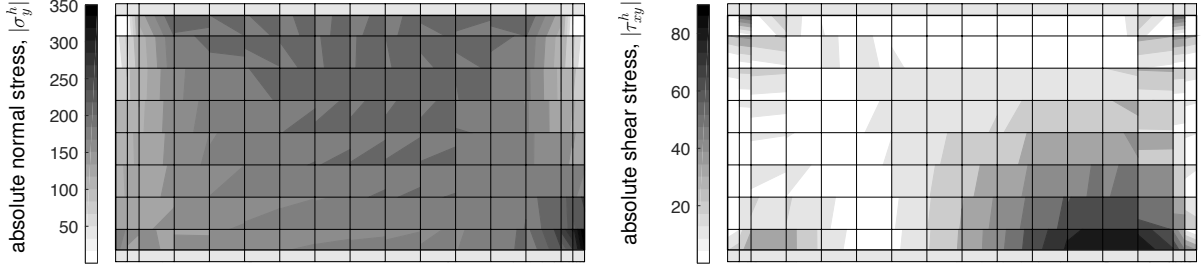


Figure 17: Sliding block problem, mesh I: contour maps of absolute normal and shear stresses.

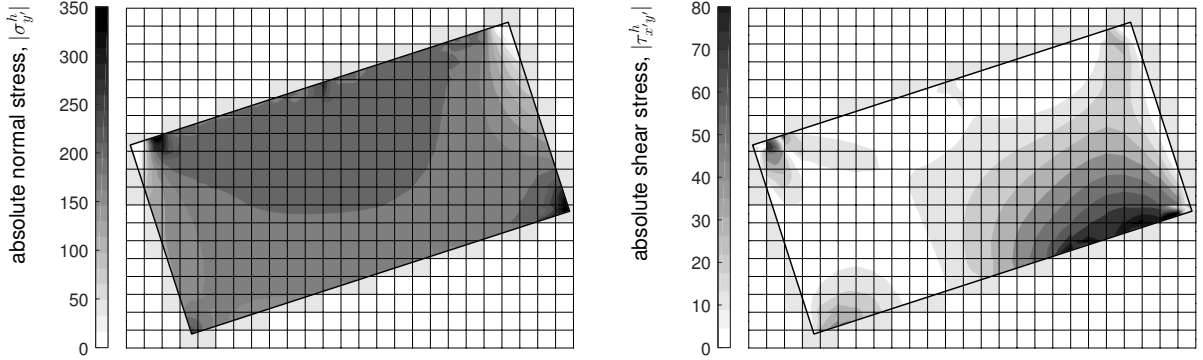


Figure 18: Sliding block problem, mesh II: contour maps of absolute normal and shear stresses.

545 The Dirichlet boundary conditions are imposed using a step size of $\epsilon = 1 \times 10^{-6}$.

31 Fig. 17 shows contour maps of vertical normal and shear stresses, σ_y^h and τ_{xy}^h , respectively
 32 in absolute values. For the purpose of validation, we plot the normal pressure $t_n = -\sigma_y^h$ and the
 33 shear traction $t_\tau = \tau_{xy}^h$ along the boundary in Fig. 16(a) (illustrated using cross markers for this
 34 mesh) as well as the result reproduced from [61], which gives good agreement in both directions,
 35 and the normal and shear tractions are computed from nodal displacements. Fig. 16(b) shows
 36 convergence during seven iteration steps, using a tolerance of $tol = 1 \times 10^{-8}$ for the normalised
 37 out-of-balance residual (40).
 38
 39
 40

41 The results of another test that employs 8-noded square elements are also shown in Fig.
 42 16, displayed with circular markers, which converges in eight iterations. The block model is
 43 rotated by 18° and immersed in a relative fine background mesh II with element size $h = 0.18\text{m}$.
 44 Corresponding contour maps of normal and shear stresses in rotated local coordinates, $\sigma_{y'}^h$ and
 45 $\tau_{x'y'}^h$, and, in absolute values are shown in Fig. 18, which gives similar stress distributions as in
 46 Fig. 17. Moreover, an illustration of r_n/r_τ of the sampling points along the frictional boundary,
 47 obtained after the first iteration (where the frictional boundary is treated as fully fixed), is
 48 plotted in Fig. 19(a). The ratio result of mesh II displays oscillation for $x \in [1.2, 1.4]$, as this is
 49 where r_τ approaches zero with the sign flipped subsequently. Fig. 19(b) shows the reciprocal
 50 of the above ratio in this area, which does not fluctuate. The contribution of reactions at ①,
 51 which deviates from the trend, is relatively small compared to, e.g., ② and ③, as shown in the
 52 inset table. Apart from this area, the plot demonstrates a generally smooth distribution of the
 53 ratio of r_n/r_τ for quadratic elements, which allows the stick-slip status to be determined at the
 54 sampling points. This test, which employs quadratic elements and constructed with the feature
 55
 56
 57
 58
 59
 60
 61
 62
 63
 64
 65

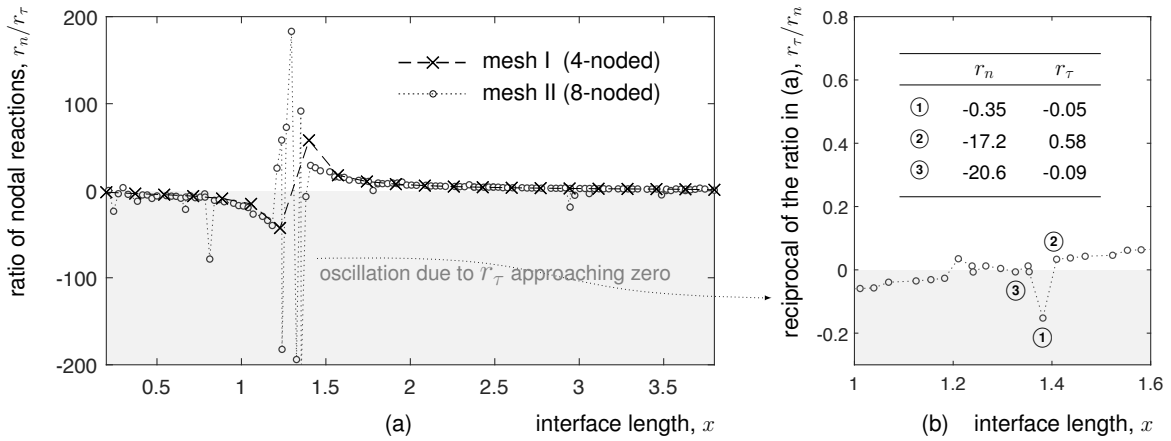


Figure 19: Sliding block problem: ratios between the normal and tangential components of nodal reactions along the frictional boundary.

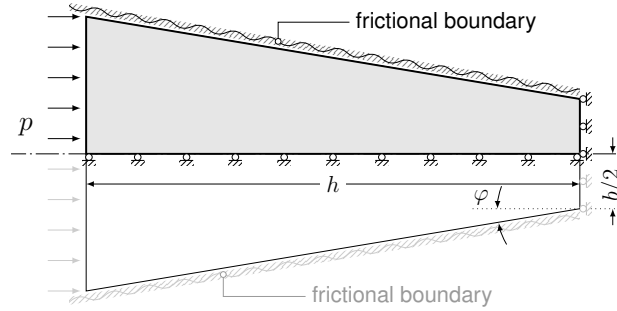


Figure 20: Problem setting of the compressed wedge and the computational model of the top half (the grey area) with boundary conditions.

of an inclined frictional boundary, has demonstrated the ability of the proposed algorithm to converge to a correct deformed state.

7.4. Wedge with frictional boundaries

In this example, the plane strain compression of a wedge into a frictional rigid shell is modelled, as shown in Fig. 20, where $h = 5\text{m}$, $b = 2\text{m}$ and $\varphi = 10^\circ$. The wedge is assumed to be linear isotropic elastic with $E = 1\text{GPa}$ and $\nu = 0.3$, subjected to an external pressure of $p = 8 \times 10^5\text{kPa}$. Only the top half is modelled due to symmetry, with a roller boundary being placed at the bottom of the computational domain and a frictional boundary at the top, where the classical Coulomb's friction law is applied. The problem is discretised in the fictitious domain using biquadratic square elements with side length $h = 0.13\text{m}$.

The problem is computed with the friction coefficient being $\mu = 0, 0.2, 0.4, 0.6, 0.8, 1.0$ and $\mu \rightarrow +\infty$, and all calculations reach final solutions after several iterations, as shown in Fig. 21(b), with a tolerance of 1×10^{-8} . Dirichlet boundary conditions in all cases are imposed using a step size of $\epsilon = 1 \times 10^{-6}\text{m}$. The comparison between stress distributions of the cases of $\mu = 0$ and 1.0 is shown in Fig. 21(a), where the von-Mises contour displays concentration on the frictional boundary near the open end, and is relatively even in the frictionless case.

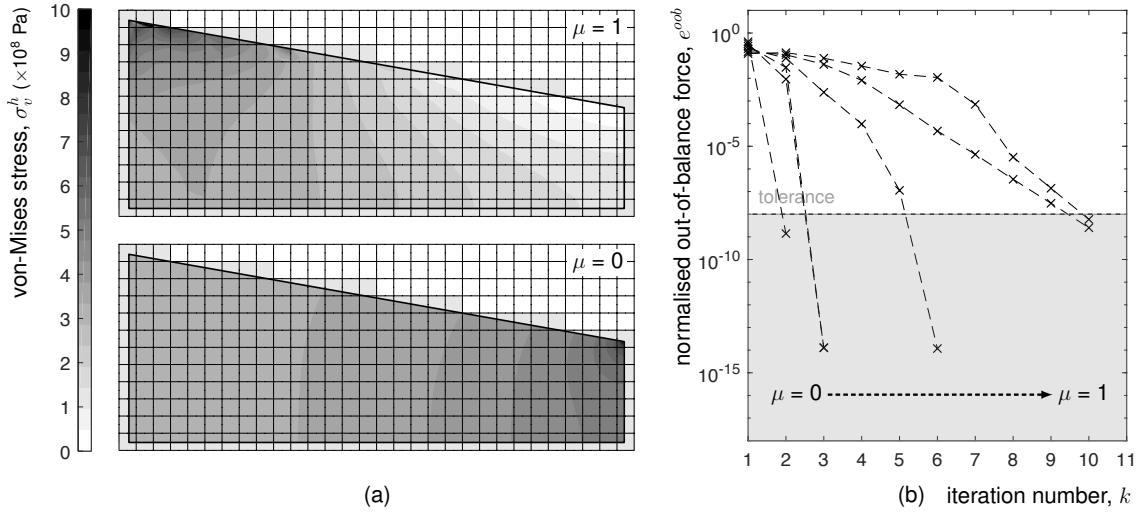


Figure 21: The wedge compression problem: (a) von-Mises stress contours with $\mu = 0$ and 1.0 and (b) normalised out-of-balance force residual versus iteration number.

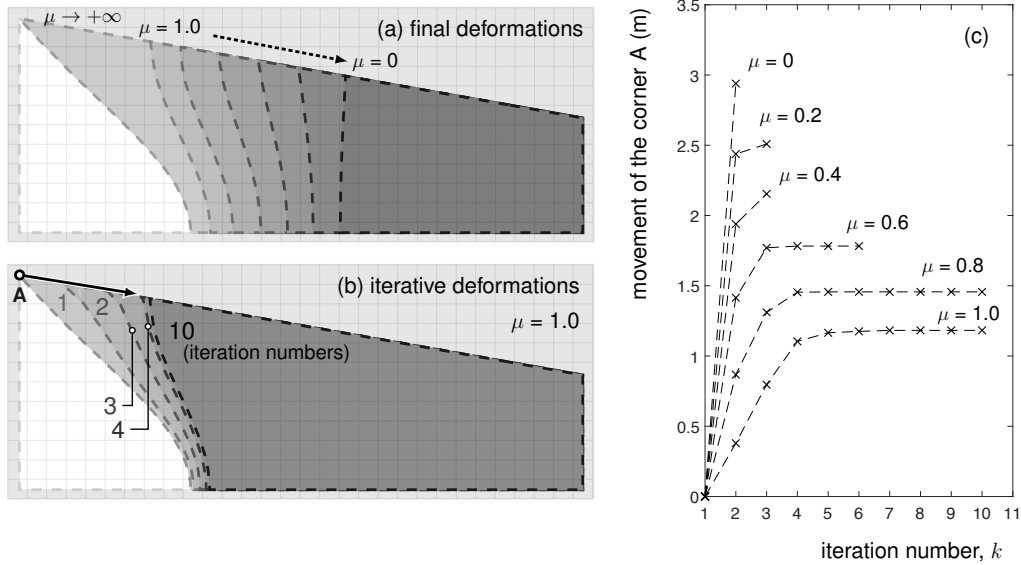


Figure 22: The wedge compression problem: (a) final deformations with $\mu = 0, 0.2, 0.4, 0.6, 0.8, 1.0$ and $\mu \rightarrow +\infty$, (b) iterative deformations of the $\mu = 1.0$ case, and (c) movement of the corner A versus iteration number in all cases.

Final deformations of all cases are shown in Fig. 22(a), where the nearly vertical free edge of $\mu = 0$ recovers the frictionless behaviour, the frictional boundary remains fully fixed for a large $\mu \rightarrow +\infty$, and other frictional sliding boundary conditions have provided more realistic interfaces for these rough sliding boundaries.

Fig. 21(b) also shows that it takes more iteration steps for a rough boundary to converge. The computation of $\mu = 1.0$ completes in 10 iterative steps, though the wedge has closely reached the final deformation in 4 iterations, as shown in Fig. 22(b), and the movement of the corner A is plotted in Fig. 22(c) against the iteration number.

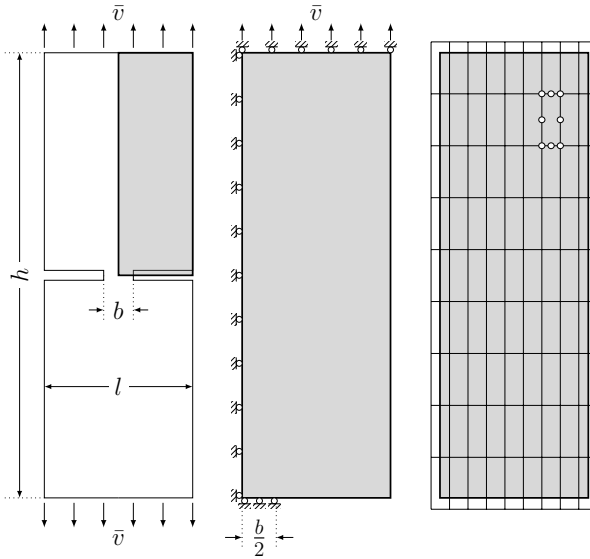


Figure 23: Computational model of the double-notched tensile specimen with boundary conditions and the initial grid.

7.5. Notched tensile specimen

This example presents the elasto-plastic analysis of the plane strain stretching of a double-notched specimen, as shown in Fig. 23. Initially presented by Nagtegaal et al. [64] to demonstrate the spurious response of standard finite elements in plasticity, it was subsequently re-analysed in a number of articles [55, 65, 66]. The total height and width of the specimen are $h = 30\text{mm}$ and $l = 10\text{mm}$, respectively, with a linking ligament $b = 2\text{mm}$ at mid height. The specimen has a Young's modulus of $E = 206.9\text{GPa}$ and a Poisson's ratio of $\nu = 0.29$, modelled using an elastic-perfectly plastic Prandtl-Reuss (P-R) constitutive model with yield stress of $\sigma_y = 0.45\text{GPa}$. The exact P-R model implementation of Wei et al. [67], which eliminates the error associated with implicit stress integration, is employed. Due to symmetry, one quarter of the specimen is initially discretised using biquadratic rectangular elements of size $0.31\text{mm} \times 0.8\text{mm}$, with reduced four-point integration for full elements and reduced single-point integration for triangular patches in cut elements. Roller boundary conditions are imposed using the step boundary method with the step size $\epsilon = 1 \times 10^{-6}\text{mm}$ throughout, including the normal pre-
605 prescription of $\bar{v} = 0.2\text{mm}$ on the top rollers in 20 equal displacement-controlled increments. The global tolerance on the Newton-Raphson process is set to 1×10^{-8} in all elasto-plastic analyses in this article.

Table 1: Notched plate convergence of the step boundary method implementation with von-Mises constitutive model.

NR iteration	loadstep			
	5	6	7	8
1	5.640×10^{-2}	2.098×10^{-2}	2.917×10^{-2}	1.037×10^{-3}
2	1.967×10^{-3}	2.193×10^{-3}	2.243×10^{-4}	1.189×10^{-6}
3	1.305×10^{-6}	8.302×10^{-6}	2.455×10^{-7}	2.066×10^{-12}
4	1.716×10^{-12}	2.227×10^{-10}	1.664×10^{-13}	-

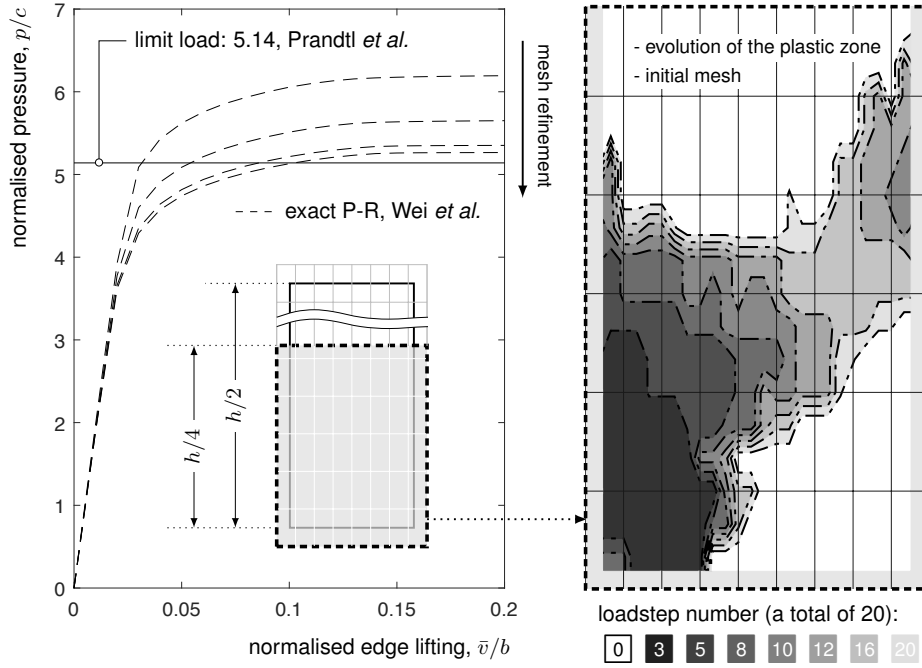


Figure 24: Normalised pressure (computed from the total reaction) against normalised edge lifting and the evolution of the plastic zone of the notched tensile specimen.

The normalised pressure against displacement response of the computation converges to the analytical solution with uniform grid refinement (where elements are halved in each refinement), as shown on the left of Fig. 24. The analytical limit load of the problem under the perfect plasticity hypothesis, which is based on slip-line theory, is given by Prandtl and Hill [56] as

$$p/\sigma_y = 2 + \pi \cong 5.14, \quad (60)$$

where $p = 2R/b$ is the normalised pressure, with R being the total reaction on the normally prescribed edge. The evolution of the yielded region obtained with the initial grid (element size of $0.31\text{mm} \times 0.8\text{mm}$) in respect of a selection of loadsteps is shown on the right of Fig. 24, and the out-of-balance force values during the global Newton-Raphson process for loadsteps 5 through 8 is provided in Table 1, which approaches optimum (2nd order) convergence of the global Newton process. These aspects validate the derivation and implementation of the step boundary finite element method for elastic-perfect plasticity.

7.6. Strip-footing collapse analyses

7.6.1. Frictionless interface

The final problem is a rigid strip footing analysis under plane strain, which tests the method using non-uniform background discretisation. The footing has a width of $b = 1\text{m}$. The soil domain has a length of $l = 10\text{m}$ and a height of $h = 5\text{m}$, and due to symmetry only half of the domain is discretised using 8-noded quadrilateral elements, integrated with reduced four-point quadrature for full elements and reduced single-point quadrature for triangular patches in cut

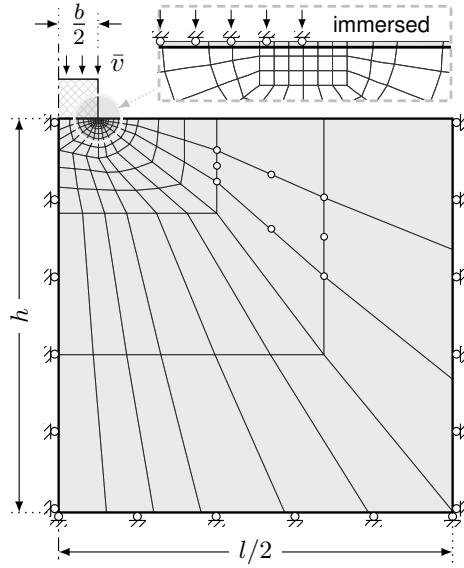


Figure 25: Computational model of the strip-footing collapse with frictionless boundary conditions.

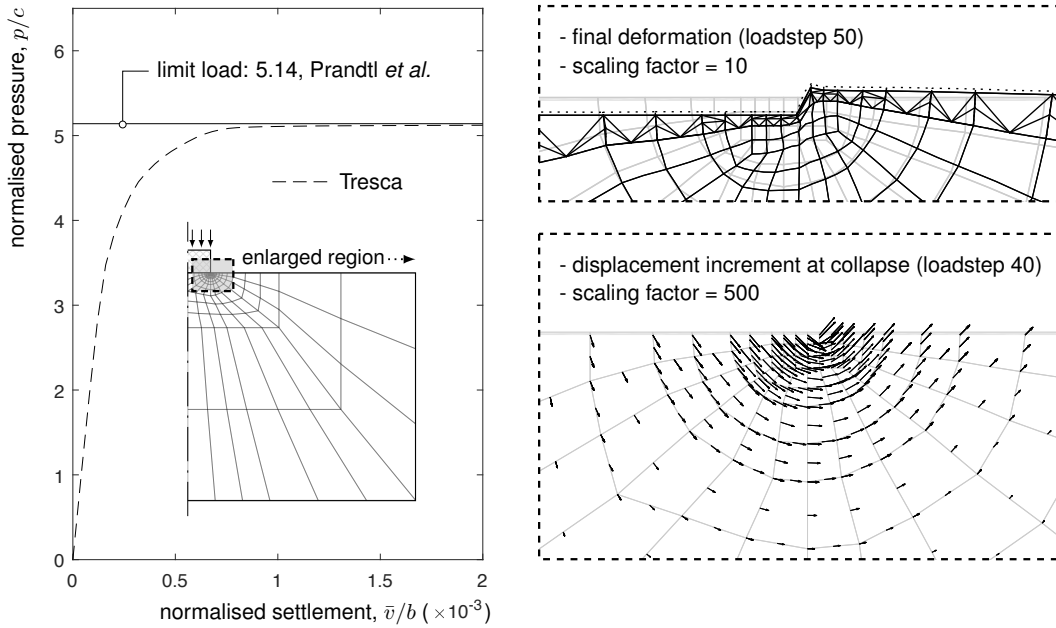


Figure 26: Frictionless strip-footing with the Tresca model: normalised pressure (computed from the total reaction) against normalised settlement, final deformation and incremental displacement at loadstep 40

elements. The same non-uniform mesh as in [55, 68] is adopted here, except that the mesh is slightly scaled in the vertical direction by a factor of 1.001 such that top edge of the soil becomes immersed in the mesh, as shown in Fig. 25.

The weightless soil is modelled as an elastic isotropic material with a Young's modulus of $E = 10\text{GPa}$ and a Poisson's ratio of $\nu = 0.48$ prior to the yield point, and the yielding is first assumed to be governed by the Tresca yield criterion with no hardening, where the yield

Table 2: Frictionless strip-footing convergence of the step boundary method implementation with the Tresca constitutive model.

NR iteration	loadstep			
	11	12	13	14
1	9.499×10^{-3}	1.933×10^{-2}	2.926×10^{-3}	4.544×10^{-3}
2	1.169×10^{-3}	1.338×10^{-3}	1.627×10^{-4}	1.342×10^{-4}
3	1.203×10^{-4}	4.695×10^{-5}	1.381×10^{-6}	5.237×10^{-8}
4	4.241×10^{-7}	1.941×10^{-6}	1.464×10^{-10}	3.004×10^{-13}
5	7.476×10^{-12}	2.743×10^{-11}	-	-

stress is taken as $\sigma_y = 848.7\text{kPa}$. The roller boundary conditions are imposed using the step boundary method with $\epsilon = 1 \times 10^{-6}\text{m}$, with the rollers on the top also being subjected to a settling of $\bar{v} = 20\text{mm}$ over 50 equal displacement-controlled loadsteps. The footing analysis is basically the compression version of the notched specimen problem presented in the previous section, and shares the same analytical limit load (60) for the Tresca material. On the left of Fig. 26 the normalised stress versus settlement response is plotted, where the result has a good agreement compared to the analytical limit. The upper-right plot in Fig. 26 displays the scaled final deformation around the rigid footing, in which the outside part of cut elements are shown by fine dotted lines, and the lower-right of Fig. 26 shows the scaled incremental displacement at collapse. Table 2 provides the global out-of-balance force values for loadsteps 11 through 14, which approaches optimum convergence in the global Newton-Raphson process.

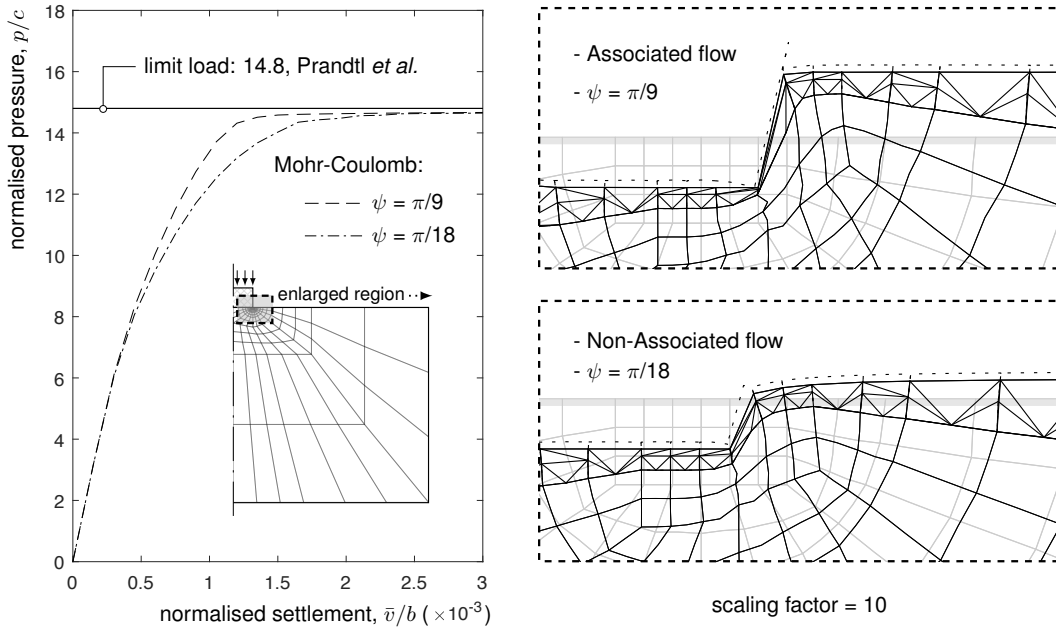


Figure 27: Frictionless strip-footing with M-C associated and non-associated flows: normalised pressure (computed from the total reaction) against normalised settlement and scaled deformations.

The rigid footing problem is also analysed using the Mohr-Coulomb (M-C) yield criterion. Fig. 27 gives the normalised pressure versus settlement response for a perfectly plastic M-

Table 3: Frictionless strip-footing convergence of the step boundary method implementation with the M-C associated and non-associated models.

NR iteration	loadstep (associated)		loadstep (non-associated)	
	4	5	4	5
1	2.470×10^{-1}	1.238×10^{-1}	1.670×10^{-1}	1.117×10^{-1}
2	3.330×10^{-2}	2.856×10^{-2}	3.677×10^{-2}	3.428×10^{-2}
3	4.089×10^{-3}	5.090×10^{-3}	1.754×10^{-3}	7.509×10^{-3}
4	4.555×10^{-6}	3.909×10^{-4}	7.150×10^{-6}	1.587×10^{-5}
5	4.634×10^{-11}	1.236×10^{-7}	4.210×10^{-10}	9.650×10^{-9}
6	–	9.601×10^{-14}	–	–

C model with cohesion of $c = 490\text{kPa}$ and a friction angle of $\alpha = \pi/9$ for both associated ($\psi = \pi/9$) and non-associated ($\psi = \pi/18$) plastic flow, where ψ denotes the dilation angle. The same mesh and elastic material properties used for the Tresca analysis are used but in this case a displacement of 3mm is imposed using 20 equal displacement-controlled loadsteps. Good agreement is observed between the two plasticity approaches and the analytical limit pressure of

$$2p/\sigma_y \cong 14.84,$$

provided by Prandtl et al. [56], and as shown by the solid black line. Table 3 provides the global out-of-balance force values for loadsteps 4 and 5 for both associated and non-associated models, which shows correct convergence in the global Newton-Raphson process. On the right of Fig. 27 the scaled deformations around the footing for associated (top) and non-associated (bottom) plastic flow are shown. The associated flow case exhibits excessive volumetric dilation in the region adjacent to the footing leading to unrealistic heaving of the ground surface. Employing a non-associated model, which has a reduced dilation angle from $\pi/9$ to $\pi/18$, significantly reduces the heave and leads to a more realistic surface profile, while the value of the yielding plateau in the pressure versus settlement response remains unvaried.

7.6.2. Frictional interface

We now consider a same footing model as in the preceding section, except that the interaction between the footing and the soil follows Coulomb's friction law. The M-C plastic model with non-associated plastic flow is adopted, where $\psi = \pi/18$ and a displacement of 3mm is imposed in 20 equal loadsteps. As the normal pressure along the interface in this footing problem is eminently greater than the tangential traction, we have selected small friction coefficients, $\mu = 0.4 \times 10^{-11}$, 0.8×10^{-11} , 1.2×10^{-11} , 1.6×10^{-11} , 2×10^{-11} and $\mu \rightarrow +\infty$, in order to observe the stick-slip behaviour. Reasonable horizontal movement of interfacial points, as shown and compared with the frictionless case in Fig. 28, is observed, while the normalised pressure result during loading does not show significant difference. A selection of the out-of-balance residual during the global Newton process is provided in Table 4. The feature of a frictional boundary has an evident effect on the rate of convergence in that more iterations are required in each loadstep, and the optimum rate of convergence is weakened due to the inconsistent tangent stiffness as discussed earlier in the article.

To summarise, these cases have demonstrated the implementation of the step boundary finite element method in elasto-plastic analysis, with features of the non-uniform background mesh,

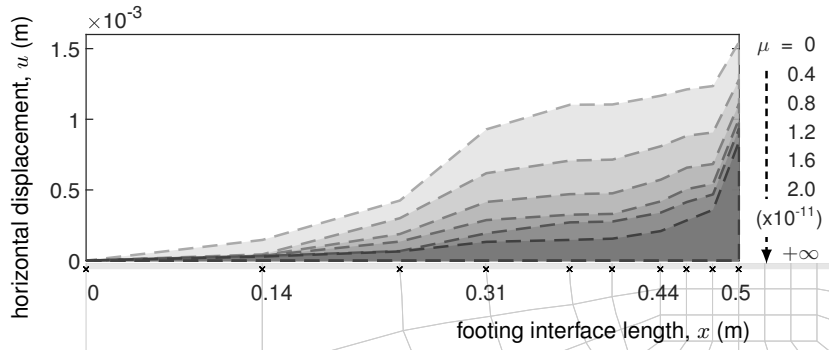


Figure 28: Total horizontal displacements on the footing interface with different interface roughness; crosses represent intersections between the grid and geometry where displacements are computed.

Table 4: Frictional strip-footing convergence of the step boundary method implementation with the M-C non-associated model.

NR iteration	loadstep ($\mu = 0.4 \times 10^{-11}$)		loadstep ($\mu = 2.0 \times 10^{-11}$)	
	4	5	4	5
1	9.563×10^{-1}	9.282×10^{-1}	9.574×10^{-1}	9.398×10^{-1}
2	6.046×10^{-2}	8.039×10^{-2}	4.834×10^{-2}	7.807×10^{-2}
3	1.466×10^{-2}	1.289×10^{-2}	1.248×10^{-2}	9.204×10^{-3}
4	1.800×10^{-2}	2.931×10^{-3}	3.093×10^{-2}	8.266×10^{-4}
5	3.044×10^{-3}	2.618×10^{-5}	3.274×10^{-3}	5.219×10^{-6}
6	4.761×10^{-4}	1.493×10^{-6}	1.300×10^{-3}	8.344×10^{-10}
7	1.494×10^{-4}	3.364×10^{-11}	1.272×10^{-4}	—
8	8.052×10^{-6}	—	9.975×10^{-6}	—
9	3.006×10^{-8}	—	4.204×10^{-8}	—
8	3.266×10^{-13}	—	8.467×10^{-13}	—

pressure-sensitive yield criteria, non-associated plastic flow and the frictional boundary.

8. Conclusions

The step boundary method allows Dirichlet boundary conditions to be imposed weakly in fictitious domain approaches which have been of interest in recent years. The complete derivation provided in this article generalises the original formulation to inclined roller boundary conditions, along with simplified stiffness matrices. The method is then extended to deal with frictional sliding boundary conditions in an iterative procedure, and validated with a Coulomb friction model. The proposed step boundary method is also studied for elasto-plasticity, with a number of numerical examples being provided. The plasticity analyses are tested using metal plasticity and pressure-sensitive soil plasticity models, and a constitutive model with non-associated plastic flow, all displaying good performance compared to analytical solutions.

Further extension to this work could be to introduce higher order approximations for the boundary and adaptive refinement for cut element integration, to increase accuracy. The work could also be extended to model contact for different physical domains, or collision in dynamic problems.

Acknowledgements

The authors gratefully acknowledge the financial support from the China Scholarship Council. The second and third authors acknowledge the support of the Engineering and Physical Sciences Research Council grant number [EP/M000397/1].

References

- [1] T. Belytschko, Y. Krongauz, D. Organ, M. Fleming, P. Krysl, Meshless methods: an overview and recent developments, *Computer methods in applied mechanics and engineering* 139 (1-4) (1996) 3–47.
- [2] C. S. Peskin, Flow patterns around heart valves: a numerical method, *Journal of computational physics* 10 (2) (1972) 252–271.
- [3] C. S. Peskin, The immersed boundary method, *Acta numerica* 11 (2002) 479–517.
- [4] R. Glowinski, T.-W. Pan, J. Periaux, A fictitious domain method for Dirichlet problem and applications, *Computer Methods in Applied Mechanics and Engineering* 111 (3-4) (1994) 283–303.
- [5] H. Johansen, P. Colella, A Cartesian grid embedded boundary method for Poisson’s equation on irregular domains, *Journal of Computational Physics* 147 (1) (1998) 60–85.
- [6] E. Burman, S. Claus, P. Hansbo, M. G. Larson, A. Massing, CutFEM: Discretizing geometry and partial differential equations, *International Journal for Numerical Methods in Engineering* 104 (7) (2014) 472–501.
- [7] A. V. Kumar, S. Padmanabhan, R. Burla, Implicit boundary method for finite element analysis using non-conforming mesh or grid, *International Journal for Numerical Methods in Engineering* 74 (9) (2008) 1421–1447.
- [8] J. Parvizian, A. Düster, E. Rank, Finite cell method, *Computational Mechanics* 41 (1) (2007) 121–133.
- [9] T. Fries, S. Omerović, D. Schöllhammer, J. Steidl, Higher-order meshing of implicit geometries—part i: Integration and interpolation in cut elements, *Computer Methods in Applied Mechanics and Engineering* 313 (2017) 759–784.
- [10] I. Babuška, The finite element method with Lagrangian multipliers, *Numerische Mathematik* 20 (3) (1973) 179–192.
- [11] H. J. Barbosa, T. J. Hughes, The finite element method with Lagrange multipliers on the boundary: circumventing the Babuška-Brezzi condition, *Computer Methods in Applied Mechanics and Engineering* 85 (1) (1991) 109–128.
- [12] Y. Lu, T. Belytschko, L. Gu, A new implementation of the element free Galerkin method, *Computer methods in applied mechanics and engineering* 113 (3-4) (1994) 397–414.
- [13] I. Babuška, The finite element method with penalty, *Mathematics of computation* 27 (122) (1973) 221–228.
- [14] T. Zhu, S. Atluri, A modified collocation method and a penalty formulation for enforcing the essential boundary conditions in the element free Galerkin method, *Computational Mechanics* 21 (3) (1998) 211–222.
- [15] J. Nitsche, Über ein variationsprinzip zur lösung von Dirichlet-problemen bei verwendung von teilräumen, die keinen randbedingungen unterworfen sind, in: *Abhandlungen aus dem mathematischen Seminar der Universität Hamburg*, Vol. 36, Springer, Elsevier, 1971, pp. 9–15.
- [16] J. Freund, R. Stenberg, On weakly imposed boundary conditions for second order problems, in: *Proceedings of the Ninth Int. Conf. Finite Elements in Fluids*, Venice, 1995, pp. 327–336.
- [17] D. N. Arnold, F. Brezzi, B. Cockburn, L. D. Marini, Unified analysis of discontinuous Galerkin methods for elliptic problems, *SIAM journal on numerical analysis* 39 (5) (2002) 1749–1779.
- [18] E. Burman, P. Hansbo, Fictitious domain finite element methods using cut elements: I. a stabilized Lagrange multiplier method, *Computer Methods in Applied Mechanics and Engineering* 199 (41-44) (2010) 2680–2686.
- [19] J. Baiges, R. Codina, F. Henke, S. Shahmiri, W. A. Wall, A symmetric method for weakly imposing Dirichlet boundary conditions in embedded finite element meshes, *International Journal for Numerical Methods in Engineering* 90 (5) (2012) 636–658.
- [20] R. Codina, J. Baiges, Weak imposition of essential boundary conditions in the finite element approximation of elliptic problems with non-matching meshes, *International Journal for Numerical Methods in Engineering* 104 (7) (2015) 624–654.

- [21] A. C. Ramos, A. M. Aragón, S. Soghrati, P. H. Geubelle, J.-F. Molinari, A new formulation for imposing Dirichlet boundary conditions on non-matching meshes, *International Journal for Numerical Methods in Engineering* 103 (6) (2015) 430–444.
- [22] E. Burman, A penalty-free nonsymmetric Nitsche-type method for the weak imposition of boundary conditions, *SIAM Journal on Numerical Analysis* 50 (4) (2012) 1959–1981.
- [23] E. Burman, P. Hansbo, Fictitious domain finite element methods using cut elements: II. a stabilized Nitsche method, *Applied Numerical Mathematics* 62 (4) (2012) 328–341.
- [24] B. Maury, A fat boundary method for the Poisson problem in a domain with holes, *Journal of scientific computing* 16 (3) (2001) 319–339.
- [25] S. Bertoluzza, M. Ismail, B. Maury, Analysis of the fully discrete fat boundary method, *Numerische Mathematik* 118 (1) (2011) 49–77.
- [26] K. Lu, C. E. Augarde, W. M. Coombs, Z. Hu, Weak impositions of dirichlet boundary conditions in solid mechanics: A critique of current approaches and extension to partially prescribed boundaries, *Computer Methods in Applied Mechanics and Engineering* 348 (2019) 632 – 659.
- [27] S. Fernández-Méndez, A. Huerta, Imposing essential boundary conditions in mesh-free methods, *Computer methods in applied mechanics and engineering* 193 (12) (2004) 1257–1275.
- [28] L. V. Kantorovich, V. I. Krylov, C. D. Benster, G. Weiss, Approximate methods of higher analysis, *Physics Today* 13 (1) (1960) 74–76.
- [29] Z. Zhang, A. V. Kumar, Immersed boundary modal analysis and forced vibration simulation using step boundary method, *Finite Elements in Analysis and Design* 126 (2017) 1–12.
- [30] I. Y. Kharrik, On approximation of functions that have zero values and derivatives on domain boundary by special functions, *Siberian mathematical journal* 4 (2) (1963) 408–425.
- [31] V. L. Rvachev, T. I. Sheiko, R-functions in boundary value problems in mechanics, *Appl. Mech. Rev* 48 (4) (1995) 151–188.
- [32] V. Shapiro, I. Tsukanov, Implicit functions with guaranteed differential properties, in: *Proceedings of the fifth ACM symposium on Solid modeling and applications*, ACM, 1999, pp. 258–269.
- [33] K. Höllig, C. Apprich, A. Streit, Introduction to the Web-method and its applications, *Advances in Computational Mathematics* 23 (1-2) (2005) 215–237.
- [34] K. Höllig, U. Reif, J. Wipper, Weighted extended B-spline approximation of Dirichlet problems, *SIAM Journal on Numerical Analysis* 39 (2) (2001) 442–462.
- [35] W. Zhang, L. Zhao, Exact imposition of inhomogeneous Dirichlet boundary conditions based on weighted finite cell method and level-set function, *Computer Methods in Applied Mechanics and Engineering* 307 (2016) 316–338.
- [36] A. V. Kumar, R. Burla, S. Padmanabhan, L. Gu, Finite element analysis using nonconforming mesh, *Journal of Computing and Information Science in Engineering* 8 (3) (2008) 031005.
- [37] R. K. Burla, A. V. Kumar, Implicit boundary method for analysis using uniform B-spline basis and structured grid, *International Journal for Numerical Methods in Engineering* 76 (13) (2008) 1993–2028.
- [38] R. K. Burla, A. V. Kumar, B. V. Sankar, Implicit boundary method for determination of effective properties of composite microstructures, *International Journal of Solids and Structures* 46 (11-12) (2009) 2514–2526.
- [39] A. V. Kumar, P. S. Periyasamy, Mesh independent analysis of shell-like structures, *International Journal for Numerical Methods in Engineering* 91 (5) (2012) 472–490.
- [40] M. Cortis, W. Coombs, C. Augarde, M. Brown, A. Brennan, S. Robinson, Imposition of essential boundary conditions in the material point method, *International Journal for Numerical Methods in Engineering* 113 (1) (2018) 130–152.
- [41] Y. Bing, M. Cortis, T. Charlton, W. Coombs, C. Augarde, B-spline based boundary conditions in the material point method, *Computers & Structures* 212 (2019) 257–274.
- [42] F. Liu, R. I. Borja, Stabilized low-order finite elements for frictional contact with the extended finite element method, *Computer Methods in Applied Mechanics and Engineering* 199 (37-40) (2010) 2456–2471.
- [43] M. A. Yerry, M. S. Shephard, A modified quadtree approach to finite element mesh generation, *IEEE Computer Graphics and Applications* 3 (1) (1983) 39–46.
- [44] R. Biswas, K. D. Devine, J. E. Flaherty, Parallel, adaptive finite element methods for conservation laws,

- Applied Numerical Mathematics 14 (1-3) (1994) 255–283.
- [45] T. Rübberg, F. Cirak, A fixed-grid b-spline finite element technique for fluid-structure interaction, *International Journal for Numerical Methods in Fluids* 74 (9) (2013) 623–660. doi:10.1002/flid.3864.
- 785 [46] A. J. Lew, G. C. Buscaglia, A discontinuous-Galerkin-based immersed boundary method, *International Journal for Numerical Methods in Engineering* 76 (4) (2008) 427–454.
- [47] C. Annavarapu, M. Hautefeuille, J. E. Dolbow, A Nitsche stabilized finite element method for frictional sliding on embedded interfaces. part i: Single interface, *Computer Methods in Applied Mechanics and Engineering* 268 (2014) 417–436.
- 790 [48] N. Kikuchi, J. T. Oden, *Contact problems in elasticity: a study of variational inequalities and finite element methods*, Vol. 8, siam, 1988.
- [49] P. Wriggers, G. Zavarise, A formulation for frictionless contact problems using a weak form introduced by nitsche, *Computational Mechanics* 41 (3) (2007) 407–420.
- [50] J. Dolbow, N. Moës, T. Belytschko, An extended finite element method for modeling crack growth with frictional contact, *Computer methods in applied Mechanics and engineering* 190 (51-52) (2001) 6825–6846.
- 795 [51] A. Gravouil, E. Pierres, M. C. Baietto, Stabilized global-local X-FEM for 3d non-planar frictional crack using relevant meshes, *International Journal for Numerical Methods in Engineering* 88 (13) (2011) 1449–1475.
- [52] M. Hirmand, M. Vahab, A. Khoei, An augmented Lagrangian contact formulation for frictional discontinuities with the extended finite element method, *Finite Elements in Analysis and Design* 107 (2015) 28–43.
- 800 [53] C. Annavarapu, R. R. Settgast, S. M. Johnson, P. Fu, E. B. Herbold, A weighted Nitsche stabilized method for small-sliding contact on frictional surfaces, *Computer Methods in Applied Mechanics and Engineering* 283 (2015) 763–781.
- [54] J. C. Simo, R. L. Taylor, Consistent tangent operators for rate-independent elastoplasticity, *Computer methods in applied mechanics and engineering* 48 (1) (1985) 101–118.
- 805 [55] E. A. de Souza Neto, D. Peric, D. R. Owen, *Computational methods for plasticity: theory and applications*, John Wiley & Sons, 2011.
- [56] R. Hill, *The mathematical theory of plasticity*, Vol. 11, Oxford University Press, 1998.
- [57] W. Coombs, *Finite deformation of particulate geomaterials: frictional and anisotropic critical state elastoplasticity*, Ph.D. thesis, Durham University (2011).
- 810 [58] Y. Saad, M. H. Schultz, Gmres: A generalized minimal residual algorithm for solving nonsymmetric linear systems, *SIAM Journal on scientific and statistical computing* 7 (3) (1986) 856–869.
- [59] K. Höllig, *Finite element methods with B-splines*, SIAM, 2003.
- [60] S. P. Timoshenko, J. N. Goodier, *Theory of elasticity*, Vol. 3, McGraw-Hill, New York London, 1970.
- [61] J. Oden, E. Pires, Algorithms and numerical results for finite element approximations of contact problems with non-classical friction laws, *Computers & Structures* 19 (1) (1984) 137 – 147, special Memorial Issue.
- 815 [62] P. Wriggers, T. V. Van, E. Stein, Finite element formulation of large deformation impact-contact problems with friction, *Computers & Structures* 37 (3) (1990) 319–331.
- [63] J. C. Simo, T. Laursen, An augmented Lagrangian treatment of contact problems involving friction, *Computers & Structures* 42 (1) (1992) 97–116.
- 820 [64] J. C. Nagtegaal, D. M. Parks, J. Rice, On numerically accurate finite element solutions in the fully plastic range, *Computer methods in applied mechanics and engineering* 4 (2) (1974) 153–177.
- [65] J. Simo, C. Miehe, Associative coupled thermoplasticity at finite strains: Formulation, numerical analysis and implementation, *Computer Methods in Applied Mechanics and Engineering* 98 (1) (1992) 41–104.
- [66] W. M. Coombs, O. A. Petit, Y. G. Motlagh, NURBS plasticity: Yield surface representation and implicit stress integration for isotropic inelasticity, *Computer Methods in Applied Mechanics and Engineering* 304 (2016) 342–358.
- 825 [67] Z. Wei, D. Perić, D. Owen, Consistent linearization for the exact stress update of Prandtl-Reuss non-hardening elastoplastic models, *International Journal for Numerical Methods in Engineering* 39 (7) (1996) 1219–1235.
- 830 [68] W. M. Coombs, Y. G. Motlagh, NURBS plasticity: non-associated plastic flow, *Computer Methods in Applied Mechanics and Engineering* 336 (2018) 419–443.